EARTH SURFACE PROCESSES AND LANDFORMS
Earth Surf. Process. Landforms **44**, 1430–1448 (2019)

Published online 17 February 2019 in Wiley Online Library
(wileyonlinelibrary.com) DOI: 10.1002/esp.4586

War landform mapping and classification on the Verdun battlefield (France) using airborne LiDAR and multivariate analysis

Rémi de Matos-Machado,[1]* Jean-Pierre Toumazet,[2] Jean-Claude Bergès,[1] Jean-Paul Amat,[3] Gilles Arnaud-Fassetta,[1] François Bétard,[1] Clélia Bilodeau,[4] Joseph P. Hupy[5] and Stéphanie Jacquemot[6]
[1] Université Paris-Diderot, Sorbonne Paris Cité, UMR 8586 PRODIG, 75013 Paris, France
[2] Université Clermont Auvergne, UMR 6042 GEOLAB, CNRS, 63000 Clermont-Ferrand, France
[3] Université Paris-Sorbonne, UMR 8185 ENEC, 75005 Paris, France
[4] Université Paris-Diderot, Sorbonne Paris Cité, UMR 7533 LADYSS, 75013 Paris, France
[5] Purdue University, School of Aviation and Transportation Technology, West Lafayette, Indiana 47906, USA
[6] DRAC Grand Est, Service Régional de l'Archéologie de Metz, 57000 Metz, France

Received 6 March 2018; Revised 10 January 2019; Accepted 14 January 2019

*Correspondence to: Rémi de Matos-Machado, Université Paris-Diderot, Sorbonne Paris Cité, UMR 8586 PRODIG, 75013 Paris, France.
E-mail: remi.machado@univ-paris-diderot.fr

ESPL
Earth Surface Processes and Landforms

ABSTRACT: Acting as efficient earth-movers, soldiers can be viewed as significant geomorphological drivers of landscape change when replaced in the recent debates on Anthropocene Geomorphology. 'Polemoforms', generated by military activities, correspond with a set of human-made landforms of various sizes and geometries. They are particularly common on the World War One battlefield of Verdun (France) which ranks among the largest battles of attrition along the Western Front. The artillery bombardments and building of defensive positions in that battle significantly altered the landscape, resulting in thousands of shell craters, dugouts, and gun positions that have altered both the meso and microtopography. This paper proposes an innovative methodology to make an exhaustive inventory of these small-scale conflict-induced landforms (excluding linear features such as trenches) using a digital terrain model (DTM) acquired by airborne LiDAR on the whole battlefield. Morphometric analysis was conducted using Kohonen's self-organizing maps (SOMs) and hierarchical agglomerative clustering (HAC) in order to quantify and classify the high number of war landforms. This combined approach allowed for mapping more than one million landforms which can be classified into eight different shapes including shell craters and various soldier-made landforms (i.e. shelters, gun positions, etc.). Detection quality evaluation using field observations revealed the algorithm successfully classified 93% of shell craters and 74% of anthropologically constructed landforms. Finally, the iconographic database and map series produced will help archaeologists and foresters to better manage the historic site of Verdun, today covered by a large forest of ~10 000 ha. © 2019 John Wiley & Sons, Ltd.

KEYWORDS: LiDAR; Polemoforms; conflict archaeology; Verdun battle; Kohonen's self-organizing map; hierarchical agglomerative clustering; landform classification; semi-automatic detection

Introduction

In terms of its sudden and immediate impacts, warfare stands out as one of the most powerful geomorphic agents, and one of the most distinguishable anthropogeomorphic ones. Although its effects are not visible in all countries, warfare has caused serious disturbances across the planet, leaving lasting scars on the human and physical environment (Arnould and Simon, 1994; Hupy, 2006; Stichelbaut, 2011; Certini *et al*., 2013; Masson-Loodts, 2014; Amat, 2015; Brenot *et al*., 2017; Capps Tunwell *et al*., 2016; De Matos-Machado *et al*., 2016; Note *et al*., 2018; Poesen, 2018). As such, it fits with recent debates and reflexions about 'Anthropocene Geomorphology' (Brown *et al*., 2013; Goudie and Viles, 2016; Tarolli, 2016), considering the profound human impact on landforms and land-forming processes at the Earth's surface during recent decades or centuries. Undoubtedly, soldiers can be viewed as fast and efficient earth-movers having a major influence on geomorphic systems and associated sedimentary records, both through direct (e.g. trench excavations) and indirect actions (e.g. land clearing for military operations). On a geological timescale, the scars of war as an anthropogeomorphic agent are recent, with most of the damage associated with the advent of modern warfare in the 20th century. Precursors of modern warfare appeared earlier during the American Civil War (1861–1865), a conflict that saw the development of heavy artillery and the birth of new landforms induced by bombturbative activities (Pittmann, 2000; Hupy and Schaetzl, 2006). The advent of smokeless gunpowder and breech loading artillery, along with the industrial production capabilities of the 20th century, subsequently ushered in an era of warfare capable of rendering irreversible geomorphological changes

upon landscapes subjected to this powerful geomorphic agent. Although myriad forms of warfare disturbance exist, those rendered by explosive munitions are among the most common.

Three large craters serve as an example to the lasting footprint of explosive munitions on the landscape. The Petersburg crater in Pennsylvania, USA (60 m long, 15 m wide and 7–9 m deep) – formed on 30 July 1864 during the American Civil War (Pittmann, 2000); the Lochnagar crater in the Somme, France (80 m in diameter and 15 m deep) – formed on 1 July 1916 during the Battle of the Somme (Doyle *et al.*, 2000); and the Sedan crater in Nevada, USA (390 m in diameter and 98 m deep) – currently the largest anthropogenic crater in the world, resulting from the US nuclear test of 6 July 1962 (Hesse, 2014) – are prime examples of the destructive power of explosives on the geomorphological landscape. Thus, war gives rise to 'polemoforms' (Amat, 1987), derived from the Greek word *pólemos* (war), which describe these landforms made by military activities (Ilyès, 2006; Brantz, 2009; Stichelbaut, 2011; Brenot *et al.*, 2017; Taborelli *et al.*, 2017a; Figure 1).

The Second Indochina War (1961–1975) was one of the first conflicts to be studied from an environmental point of view (Orians and Pfeiffer, 1970; Westing and Pfeiffer, 1972; Westing, 1975; Hupy, 2011). Even if Westing, 'pioneer on the environmental impact of war' (2013), was primarily interested by the ecological consequences of chemical weapons, he paid special attention to the millions of shell craters left by US bombers, which caused forest loss and agricultural land destruction. After that, an increasing body of scientific research on conflict related landforms has been generated; in Italy (Celi, 1991), in England (Doyle and Bennett, 1997; Doyle *et al.*, 2000) but also in France where a series of works occurred on WWI (Amat, 1987, 2001; Arnould and Simon, 1994; Hupy, 2006; Hupy and Schaetzl, 2006) and WWII battlefields (Hutchinson *et al.*, 2008; Passmore *et al.*, 2013; Capps Tunwell *et al.*, 2016).

With the advent of digital technologies and in the context of WWI Centenary Celebrations, research concerning the geomorphological traces of war has gained in prominence. As one of the pioneers in this field of research, Stichelbaut's work consisted of studying the scars of 1914–1918 battles in Flanders by means of historical aerial photographs (Stichelbaut, 2009, 2011). Devos *et al.* (2015) suggested a similar approach near Reims (France) based on the use of historical maps. Taborelli *et al.* (2016) applied a comparable methodology to the Argonne forest the following year. Led by the increasing use of LiDAR in human sciences and archaeology (Devereux *et al.*, 2005; Doneus and Briese, 2011; Georges-Leroy *et al.*, 2011; Wulder *et al.*, 2012; Opitz and Cowley, 2013), Stal *et al.* (2010), Štular (2011) and Hesse (2014) proposed new forms of research to better document conflict landscapes through remote sensing. Taking advantage of these scientific advances, a LiDAR dataset was analyzed in 2014 to document and quantify the polemoforms on 70 ha of the Caures Wood, north of the Verdun battlefield (De Matos-Machado *et al.*, 2016). In 2016, Stichelbaut *et al.* (2016b) used LiDAR to examine WWI mine craters near Ypres. Kobiałka *et al.* (2016) performed a LiDAR analysis of polemoforms induced by the 1939 fighting along the Brda River (Poland). In 2016, a major book was published compiling a series of aerial archaeology studies concerning LiDAR and conflict landscapes (Stichelbaut and Cowley, 2016a). Van der Schriek and Beex (2017) published another related work where they identified WWII remnants near the town of Bussum (Netherlands) by means of LiDAR. Finally, Gheyle *et al.* (2018) proposed a LiDAR analysis of WWI polemoforms near Ypres (Belgium).

While promising, most of the above-mentioned studies are confronted with the recurring problem concerning the large number of features to be mapped, due to the industrial nature and scale of 20th century modern warfare. The objective of achieving a polemoform inventory as exhaustive as possible leads to search for different methods from those previously deployed, which were based on tedious manual digitization practices. Current research proposes two automated mapping methods related to polemoforms. Brenot *et al.* (2017) implemented a method based on the use of topographic position index over a battlefield of 30 ha in the Argonne. Magnini *et al.* (2017) suggested another automated approach using sky-view factor and multiresolution segmentation on 400 ha of battlefield near Fort Lusern (Italy), limited in its approach by only focusing on shell craters. Moreover, most of the previous body of research does not discuss the shape variability of polemoforms.

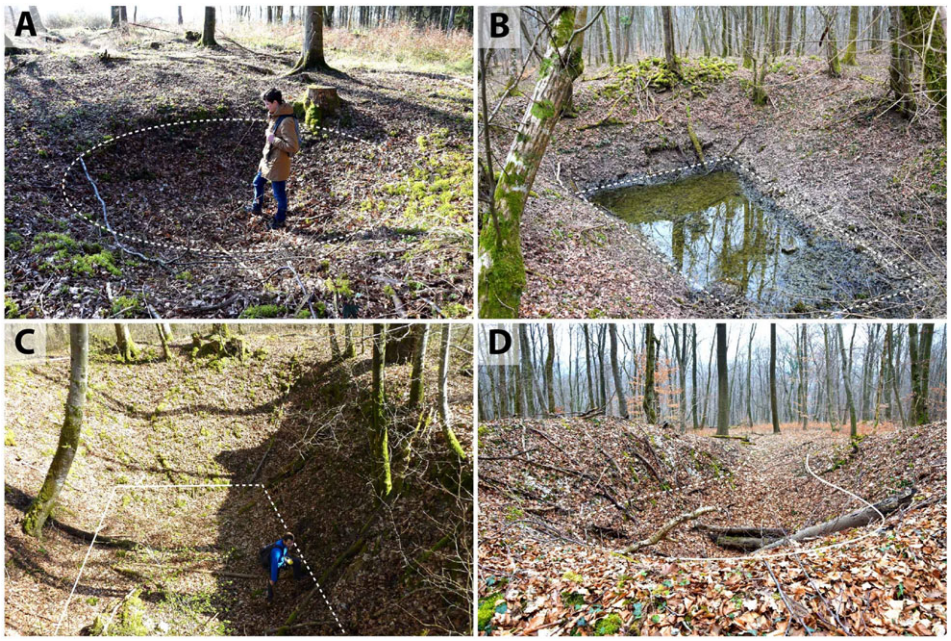

Figure 1. Four types of common landforms observed on the Verdun battlefield: (A) shell crater in the Chaume Wood (bois de Chaume – photo R. de Matos Machado, April 2017); (B) German shelter in the Haumont Wood (bois d'Haumont – photo R. de Matos Machado, March 2015); (C): installation for a German bunker in the Ormont Wood (bois d'Ormont – photo D. Jacquemot, March 2014); (D) gun position near The Tavannes Tunnel (photo R. de Matos Machado, March 2015). [Colour figure can be viewed at wileyonlinelibrary.com]

In the continuity of these works, we propose another semi-automatic method, applied on a much larger area of the Verdun battlefield comprising 100 km^2 (Figure 2). Our approach includes, after a first step of automatic detection, an automatic landform classification technique, based on morphometric analysis, allowing the identification of both simple and complex polemoforms.

Study Area

The contemporary Verdun battlefield is a vastly wooded region (9615 ha) located approximately 200 km east of Paris (Figure 2), in the department of Meuse. The study site lies on the right bank of the Meuse River, on the eastern part of the Verdun battlefield in what is today referred to as the Verdun forest (Figure 3). It is part of a cuesta relief between the heights of the Meuse valley and the town of Verdun, respectively located west and south of the forest. The western part of the study site occupies the limestone plateau of Hauts-de-Meuse, ranging between 300 and 350 m above sea level (a.s.l.), and overlooks to the east the marshy and wet depression of the Woëvre, with an altitude of 200–250 m a.s.l. The connection between the plateau and the plain is formed by a slope: the Meuse cuesta, commonly called Côtes-de-Meuse (Amat, 2001, 2015; Hupy, 2006; De Matos-Machado *et al.*, 2016).

The WWI battle of Verdun began on 21 February 1916 on the right bank of the Meuse River, where the German army surprised the French with an artillery barrage that rained between 1 and 2 million shells during the first two days of the battle. By July of 1916, that number had increased to 40 million (Solard, 1935; Pétain, 1986). Altogether, an estimated figure of 60 million shells were fired between February and December 1916, which is the official historical duration of the battle (Cochet, 2014; Prost and Krumeich, 2015). Although subsequent WWI battles witnessed even larger numbers of artillery rounds expended, Verdun remains unique for being the first to heavily implement artillery, and for its relatively compact size. A 5 km long front and 10 km deep on the right bank, extended to 20 km on the left bank from March to June 1916. Thus, the violence and the duration of the bombings and assaults on a space scarcely greater than the city of Paris have significantly scarred the landscape. Today, the image of an 'orange peel' is evoked to illustrate the chaotic relief of the battlefield (Hupy, 2006; Hupy and Schaetzl, 2006; De Matos-Machado *et al.*, 2016). Reforestation efforts, along with controversial French government policy following the war that effectively prevented farmland from being reclaimed and villages from being rebuilt, has led to a heavily forested landscape that has protected the soil from 70 years of rain and agricultural erosion (Amat, 2001; Steinbach and Husson, 2007). Unlike other WWI battlefields where the scars of war have healed with time and economic activities such as the Somme, Verdun remains unique for its preservation style memorial status. This preservation status and tree cover protecting the soil makes for an ideal situation for mapping polemoform features.

Material and Methods

Polemoform mapping was achieved using 2013 Verdun forest LiDAR data. The LiDAR dataset was used to create a Digital Terrain Model (DTM) of the research area, which allowed for identification of polemoforms through a variety of methods described in further detail below.

LiDAR dataset

This study predominantly relied upon the use of a LiDAR dataset, gathered using fixed-wing aircraft flying over the Verdun forest region on 26 and 27 March 2013 (Figure 3).

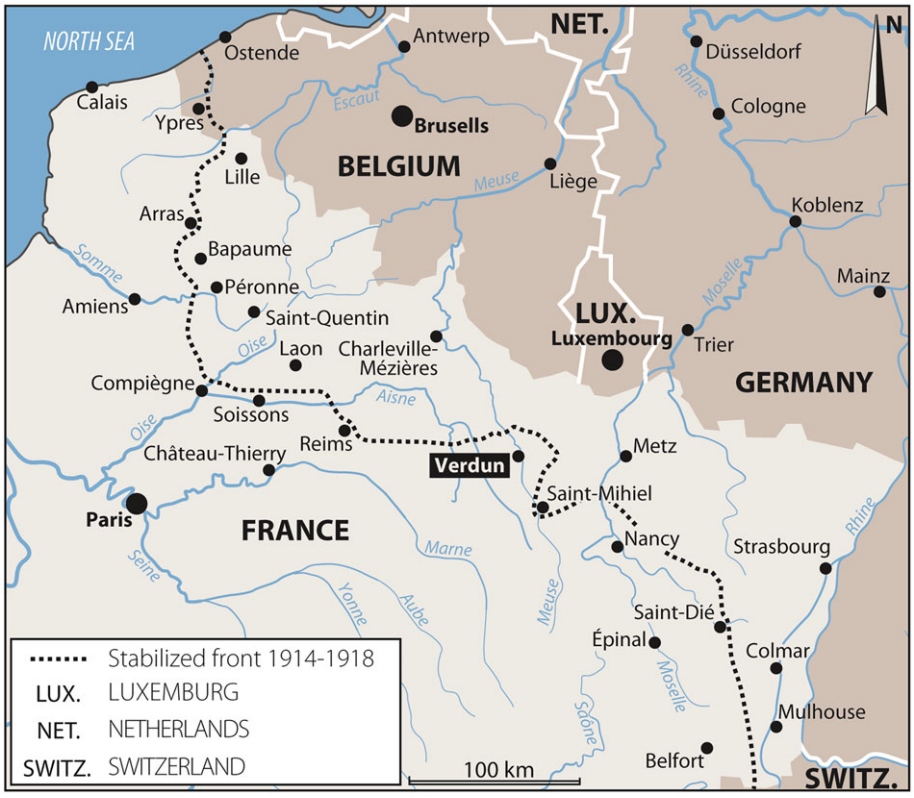

Figure 2. Location of the Verdun Battlefield on the Western Front. Winter 1914 marked the transition to a trench warfare. It resulted in a 'fixed' frontline until the last months of the conflict. [Colour figure can be viewed at wileyonlinelibrary.com]

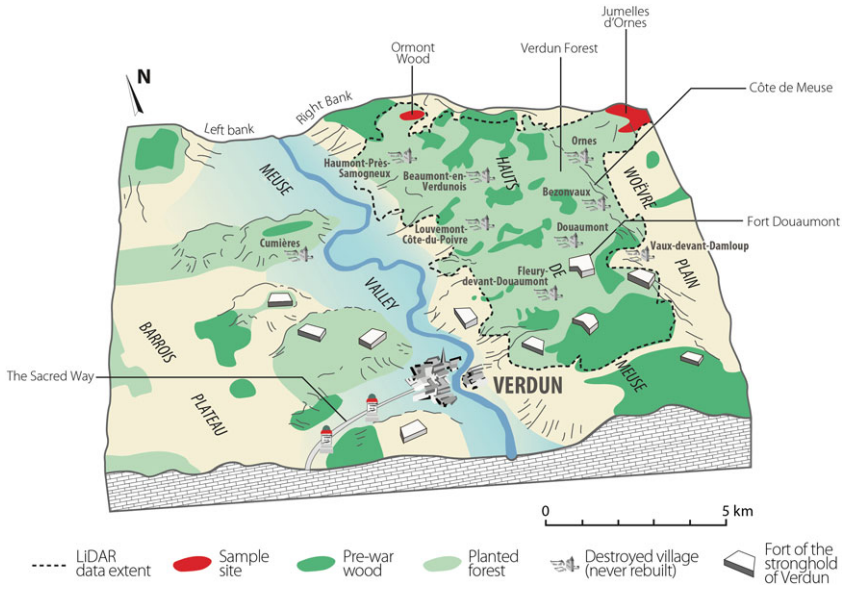

Figure 3. 3-D representation of the Verdun battlefield. [Colour figure can be viewed at wileyonlinelibrary.com]

These LiDAR missions gathered data over nearly 100 km^2 of woodland, with an average density of 44 points/m^2 recorded at the top of the canopy and 16 points/m^2 on the ground. In order to visualize the surface topography, the LiDAR point cloud was filtered to retain only the points associated to class 2, i.e. ground points according to the American Society for Photogrammetry and Remote Sensing classification (ASPRS). The filtered point-cloud was then used to generate a DTM with 20 cm ground spaced distance (GSD). This step was completed with ArcGIS® Desktop 10.5, using the natural neighbor method of the Interpolation Toolset. This method was used because of the fast results along with abilities to generate very few errors in a low relief configuration (Bater and Coops, 2009). Finally, the denoising algorithm developed by Sun *et al.* (2007) was performed using the Mesh Denoise tool in SAGA GIS® (Figure 4). Although highly detailed, not all features in the LiDAR dataset were needed; the high precision of LiDAR data acquired on the Verdun forest revealed undesirable artefacts on the DTM (i.e. branches, tree trunks, small holes, etc.). To minimize effects, the algorithm smooths the surface roughness while preserving the original appearance of the relief shapes. Its effectiveness has been demonstrated by Stevenson *et al.* (2010) on different DTMs.

Sample sites

In order to validate the method of semi-automated mapping of polemoforms, verification methods were performed on sample sites through field-based ground-truthing procedures (Figure 3). The first site (290 ha) is located on the Hauts-de-Meuse plateau at the far north of the forest, including the Ormont Wood; the second site (420 ha) occupies the Ornes Twins outlier *(Jumelles d'Ornes)*, positioned in front of the cuesta, in the Woëvre plain, a few kilometers north of the rebuilt village of Ornes. These sites were selected because of the variety of landforms at each location. The field-based ground truthing survey work was performed in March and April 2014, 2015 and 2016 when bare deciduous trees provided optimum visibility conditions. The first stage of the process was to locate via visible identification on the DTM using ArcGIS software, approximately 1100 landforms for the two test sites. Once these features were identified, a sampling map connecting each structure was drawn to facilitate navigation and data collection at the field sites. To achieve the surface survey, the sample site geographic coordinates and sampling routes were transferred to a DGPS allowing for viewing sampling schemes and LiDAR base maps in the ground-truthing phase. During this field-based procedure, observation work was carried out with archaeologists and foresters using an archeo-geomorphological approach applied in the Caures Wood (De Matos-Machado *et al.*, 2016). Thus, *in situ* analysis consisted in defining the features origin and separating soldier constructed features (i.e. trenches, shelters, gun positions) from those induced by bombings (i.e. shell craters). From these field-based surveys, 350 soldier-made excavations and 529 shell craters were mapped, representing 879 interpreted landforms (274 of the 1100 sampled landforms were not interpreted due to their excessive complexity or limited access).

War landforms extraction

Following identification of polemoforms in the field, semi-automated mapping techniques were applied to extract features on the larger DTM datasets. The extraction process involved five distinct steps (Figure 4):

i. Known foreign structures (i.e. modern roads, marked tracks, forest patches boundaries, ditches) were eliminated to keep the soldier-made landforms. This procedure was facilitated by relying on data already mapped by the Verdun's National Forests Office (ONF). Features not identified by the ONF were vectorized manually through on-screen digitization methods. A buffer zone of varying width was drawn around these objects and used as a mask. The final results were two clipped DTMs devoid of modern features above the ground surface.
ii. The local relief model algorithm (LRM; Hesse, 2010) was applied to both sites using RVT software (Kokalj *et al.*, 2011; Zakšek *et al.*, 2011; Relief Visualization Toolbox, 2015) and a kernel size of 6×6 m, which is particularly adapted to the size of the mapped landforms. This method, also known as trend removal or residual relief, separates the small landforms from the trend-surface (Hiller and Smith, 2008; Challis *et al.*, 2011; Kokalj *et al.*, 2011; Štular *et al.*, 2012). After the processing is complete, an image composed of negative and positive metric values is obtained: the negative values correspond to the concave

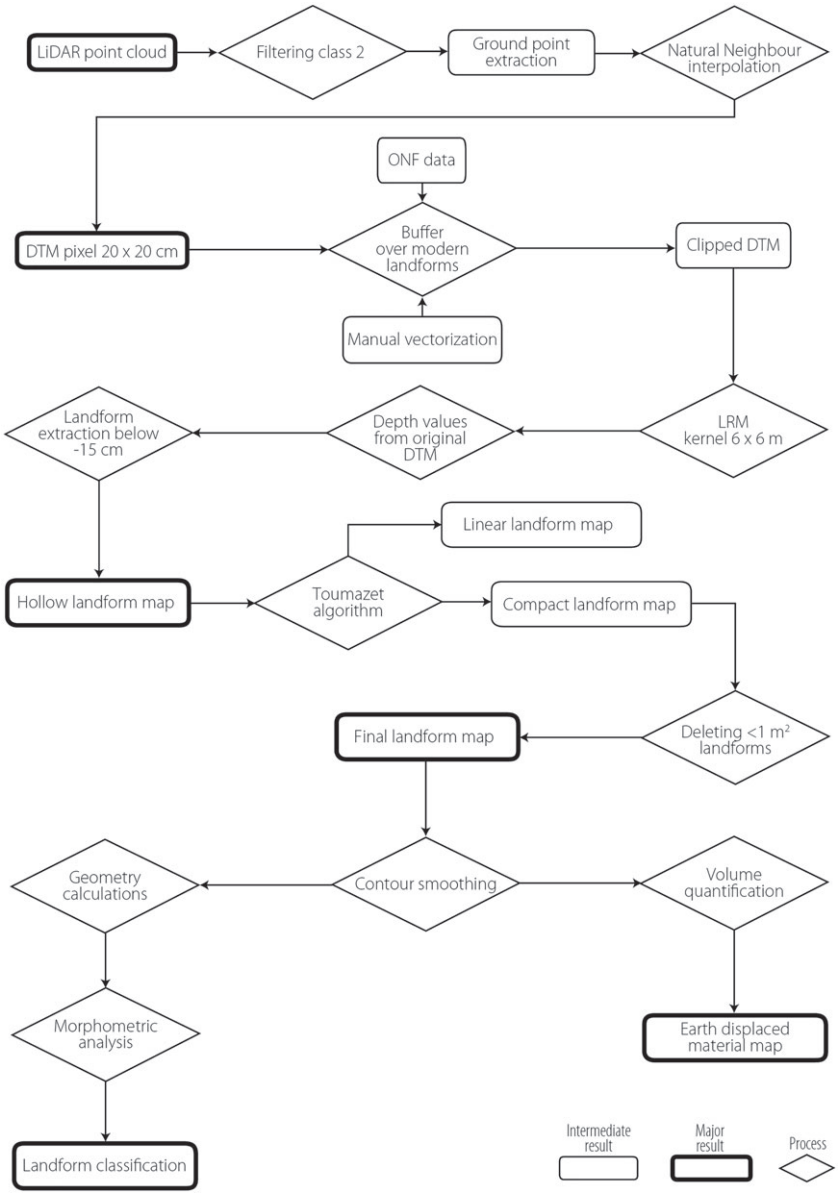

Figure 4. Processing chain for landform extraction.

reliefs, the positive values represent the convex reliefs and values close to 0 m correspond to the trend-surface (plane shapes). Thus, in addition to other visualization methods, the LRM has the great advantage of directly providing the depth or the height of the mapped objects. Despite this contribution, however, the LRM is disadvantaged to slightly smooth the landforms, especially on the slopes. As depth values are needed for the study, this parameter was calculated for each landform directly from the original DTM.

iii. A thresholding was applied to map the polemoforms. According to our observations in the field, war landforms are mostly excavated features; explosive munitions created depressions and soldiers dug beneath the surface to avoid enemy fire. Landforms resulting from shell craters and building excavation are notable as concave features. Thus, the choice was made to extract the negative values from the LRM. After several tests and on the base of the sampled sites, the landforms located below –15 cm were retained to avoid small depression extraction due to natural surface roughness.

iv. After filtering out small depressions, the algorithm developed by one of the authors (J.-P. Toumazet) was performed to separate compact and linear features. It is an adaptation of a previously developed automatic detection process (Toumazet *et al.*, 2017) and is based on bounding box measurements (Figure 5). To identify linear features, the bounding box area must correspond to at least one of the three following criteria: (i) measuring more than 20 times the size of a typical compact feature chosen as a model (to detect massive features); or (ii) measuring at least equal to half of the model bounding box area and characterized by a bounding box length/width ratio at least equal to three (to detect horizontal and vertical features); or (iii) measuring at least equal to half of the model bounding box area and with an actual surface representing less than 25% of the bounding box area (to detect diagonal features).

v. For linear features (i.e. trenches), a semi-automated method based on a skeletonization process was performed (not presented in this paper). For compact features (i.e. shell craters, shelters, gun positions, etc.), a final selection was carried out to eliminate landforms with surface $<1\ m^2$ (between 70 and 80 cm diameter) whose morphometric signal is not pronounced enough. This value corresponds to the 75 mm shell craters's minimum size observed on the field (Arnould and Simon, 1994; Amat, 2001; Hupy, 2006) that is the smallest long range shell caliber used during WWI.

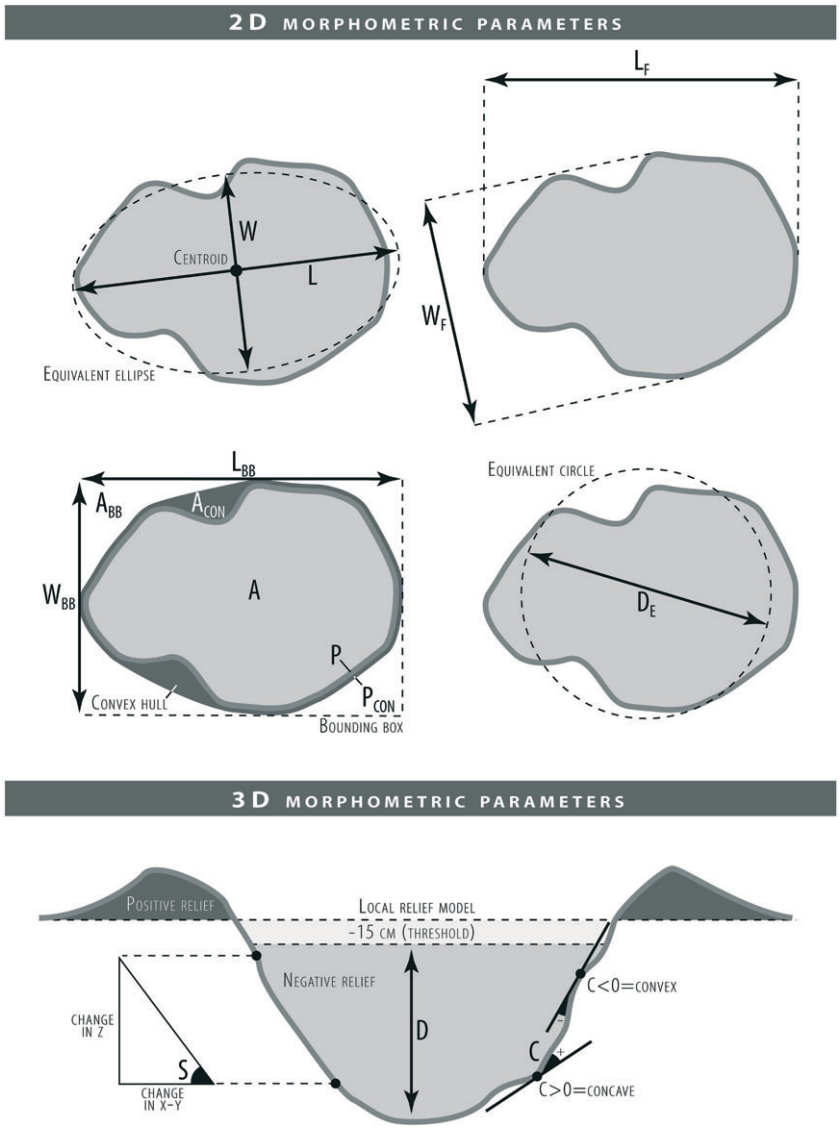

Figure 5. Landform geometry calculations.

Morphometric calculations and multivariate analysis of compact features

After identification and extraction of landforms at the two sites, landform contours were improved using the PAEK algorithm of the Smooth Polygon tool in ArcGIS® (3 m tolerance). Geometries were then calculated with Zonal Toolset of ArcGIS® and the three dimensions of the DTM (Figure 5, Tables I and II). This resulted in an elementary table describing mapped landforms in terms of 26 morphometric parameters, most of which were described by Hengl and Reuter (2009), Leibrandt and Le Pennec (2015) and Liu *et al*. (2015). For

Table I. List of basic parameters

Parameter		Symbol	Unit	Software and tool used for calculations
Area	2D	A	m^2	ArcGIS® - *Calculate geometry*
Perimeter		P	m	ArcGIS® - *Calculate geometry*
Major axis (length)		L	m	ArcGIS® - *Zonal geometry*
Minor axis (width)		W	m	ArcGIS® - *Zonal geometry*
Feret major axis		L_F	m	SAGA GIS® - *Polygon shape indices*
Feret minor axis		W_F	m	ArcGIS® - *Minimum bounding geometry*
Length of the bounding box		L_{BB}	m	ArcGIS® - *Minimum bounding geometry*
Width of the bounding box		W_{BB}	m	ArcGIS® - *Minimum bounding geometry*
Area of the bounding box		A_{BB}	m^2	ArcGIS® - *Minimum bounding geometry*
Area of the convex hull		A_{CON}	m^2	ArcGIS® - *Minimum bounding geometry*
Perimeter of the convex hull		P_{CON}	m	ArcGIS® - *Minimum bounding geometry*
Equivalent diameter		D_E	m	ArcGIS® - *Minimum bounding geometry*
Depth	3D	D	m	ArcGIS® - *Zonal statistics*
Slope		S	°	ArcGIS® - *Slope*
Profile curvature		C	m	ArcGIS® - *Curvature*

Table II. List of derived parameters

Parameter	Symbol	Formula	Unit	Signification
Miller circularity	*Cir*	$4\pi A/P^2$	0 to 1	1=circle; 0.5=polygon; 0.1=line
Rectangularity	*Rec*	A_{BB}/A	0 to 1	1=square; 0.5=polygon with concavities; 0.1=polygon with great concavities
Aspect ratio	*Asp*	W_F/L_F	0 to 1	1=circle; 0.70=square; 0.57=triangle; 0.25=elongated shapes; 0.1=line
Elongation	*E*	L_F^2/A	0 to 1	0.1=circle; 0.2=ellipse and rectangle; 0.4=elongated shapes; 0.5=line
Convexity	*Con*	P_{CON}/P	0 to 1	1=convex contour; 0.5=sinuous contour
Solidity	*Sol*	A/A_{CON}	0 to 1	1=no concavities; 0.5=concavities area equal to 50% of A
Defect area	*Def*	$(A_{CON}-A)/A$	%	0=no concavities; 50= concavities area equal to 50% of A; 100=concavities area equal to A
Percentile 90 of slope	S_{90}	-	°	10% highest values of slope
Range curvature	C_{RANGE}	-	m	C_{MAX}-C_{MIN}
Percentile 10 of curvature	C_{10}	-	m	10% lowest values of curvature
Percentile 90 of curvature	C_{90}	-	m	10% highest values of curvature

To avoid outlier values, percentiles 10 and 90 were used instead of minimum and maximum.

comparison purposes, variables benefited from a mean-centering. First, a univariate analysis was conducted to evaluate the behavior of the morphometric parameters over the whole dataset. Subsequently, a multivariate analysis was performed to classify the landforms according to their shape. This was done using the combination of Kohonen's self-organizing maps (SOMs) and hierarchical clustering (HAC), which gave the best results after comparing with principal component analysis (PCA) and K-means (using these two methods, different shapes were sometimes found within the same classes). The table analysis and classification were completed with RStudio© software using Kohonen and Stats packages (Wehrens and Buydens, 2007). Finally, volumetric content per landform was quantified using the Polygon Volume tool in ArcGIS® in order to evaluate the amount of earth materials displaced by extractive processes (Figure 4).

Kohonen's self-organizing maps proposed by Teuvo Kohonen in 1982 is a method consisting in classifying individual elements with similar characteristics into distinct classes (Oja and Kaski, 1999; Agarwal and Skupin, 2008; Ehsani and Quiel, 2009; Olteanu-Raimond and Ruas, 2015). It should be noted that the class-assignment process is nonlinear and relatively close to the K-means method with the difference that SOMs take into account a notion of topology between classes, increasing significantly the contrast between them. That is why the K-means algorithm was not used for classification. Thus, each individual is associated to a class according to its proximity to the same class individuals but also to the neighboring classes. This additional characteristic causes the contrast between dissimilar neurons to be higher than K-means. Another difference of the SOMs pertains to their two-dimensional representation space. Indeed, each class is represented graphically by a neuron containing *n* individuals, in this case the mapped landforms (Figure 6). The set forms a network called Kohonen's map. The neural network size is directly defined by the operator at the beginning of the calculation process. Neural network dimensions must be large enough so that the topological constraints can have an effect on the dataset. There is no rule that defines the grid size. Several dimensions must be tested to identify the most suitable of them. In our case, several grid sizes were used from

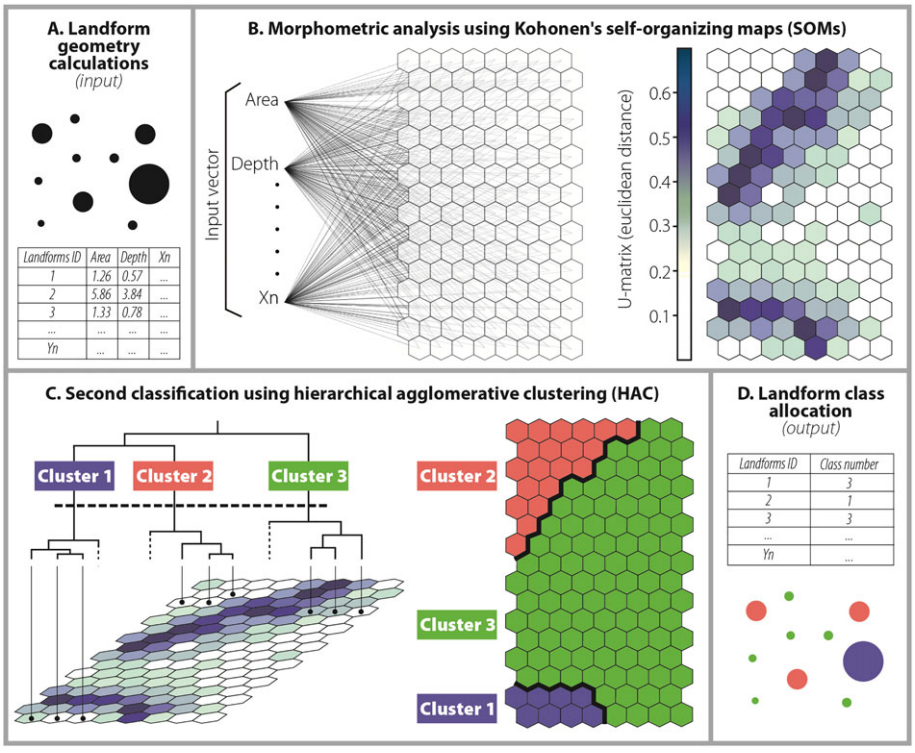

Figure 6. Morphometric analysis and landform classification using SOMs and HAC. [Colour figure can be viewed at wileyonlinelibrary.com]

10×10 to 30×30 neurons. After the process is completed, a distance matrix (U-matrix) representing the Euclidean distances between each neuron is calculated (Figure 6). It is also possible to assess the variable influence for each neuron and display the influence property into the grid independently or simultaneously. Thanks to their two-dimensional neural grid, SOMs contribute to quickly and efficiently discern the different landform geometries as shown by Agarwal and Skupin (2008) or Ehsani and Quiel (2009). Although this method facilitates the reading of such an important dataset, it provides a large number of classes. Therefore, the grid size needs to be reduced in order to acquire landform separated classes. As Olteanu-Raimond and Ruas (2015) and Unglert *et al*. (2016), this was subsequently performed using hierarchical agglomerative clustering (HAC) over Kohonen's results (Figure 6).

Because of the high number and the high diversity of landforms needing identification, three classifications were performed:

i. A first clustering (neuron grid size 30×30) based on *Asp*, *Con*, C_{90}, *Cir* and S_{90} parameters (Hengl and Reuter, 2009; Leibrandt and Le Pennec, 2015; Liu *et al.*, 2015) was applied to eliminate shell craters because of their influential weight in the dataset. Indeed, their high number produces a mass effect, which causes the other landforms to be underrepresented through misidentification.
ii. A second clustering (neuron grid size 30×30) over the remaining landforms using 3D parameters allowed detection of the constructed landforms (steep slopes) which represent the most interesting landforms in terms of history and archaeology. The combination of C_{90} and S_{90} gave the best results.
iii. A third clustering (neuron grid size 10×10) using 2D parameters (*Asp*, *Cir* and *Rec*) was performed on the results of the previous classification in order to visualize the different types of landform geometries.

Detection method validation and generalization

Field observations conducted on the two sample sites served as a means of calibration for method development. Comparison of

Table III. Averaging parameters of A clustering

Class	*Asp*	*Con*	C_{90}	*Cir*	*Sol*	S_{90}
A1	0.77	0.99	0.04	0.93	0.99	19.16
A2	0.55	0.99	0.04	0.79	0.99	18.77
A3	0.51	0.94	0.06	0.52	0.78	21.99

Table IV. Averaging parameters of B clustering

Class	C_{RANGE}	C_{90}	S_{90}
B1	0.07	0.04	15.5
B2	0.14	0.05	23.7
B3	0.20	0.07	32.1
B4	1.18	0.19	32.7

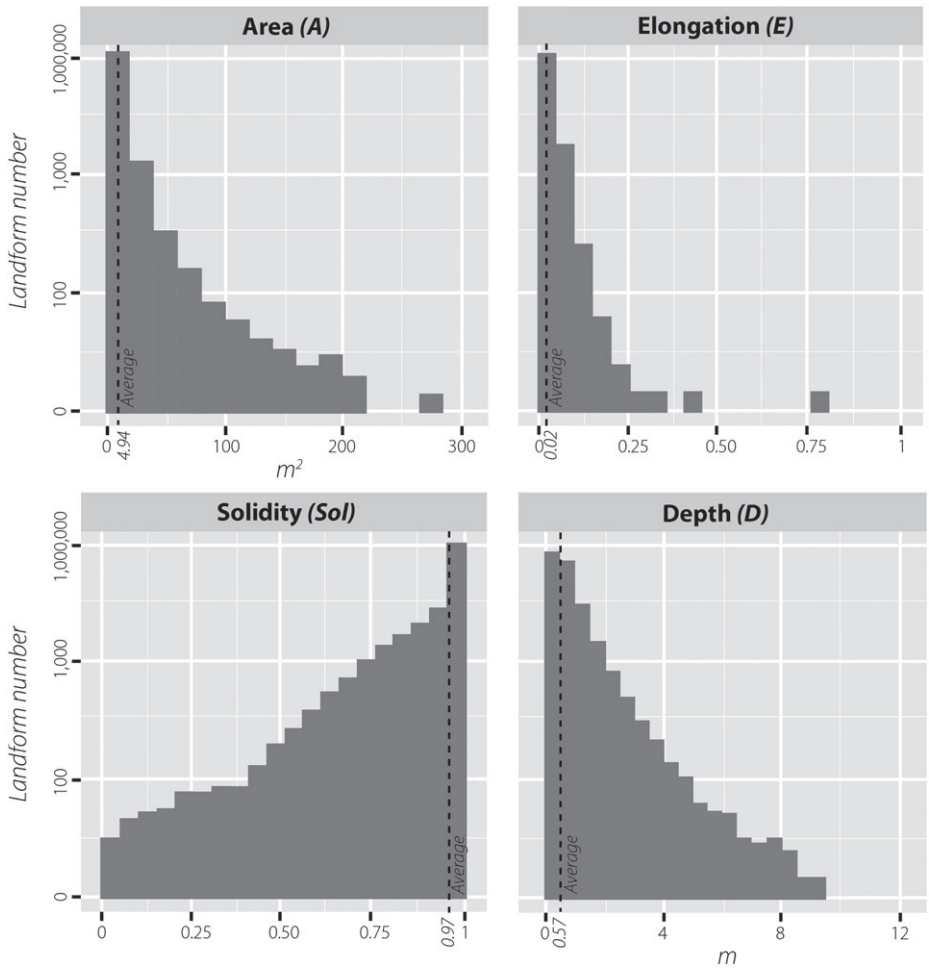

Figure 7. Histograms of four morphometric parameters.

Table V. Averaging parameters of C clustering

Class	*Asp*	*Def*	*Cir*	*Rec*
C1	0.39	22	0.51	0.62
C2	0.22	21	0.36	0.65
C3	0.67	124	0.16	0.33
C4	0.62	1	0.86	0.78
C5	0.45	6	0.68	0.72
C6	0.73	9	0.75	0.69
C7	0.48	27	0.5	0.58
C8	0.28	1	0.49	0.72
C9	0.56	73	0.31	0.43

results between craters extracted by the model and those field identified confirmed 472 shell craters (89%) of the 529 extracted by the model while 57 (11%) remain undetected. Among these landforms missed in the model extraction, 39 (68%) are flooded shell craters. In his study of the Verdun forest's ponds, Printemps (2017) showed the inefficiency of the LRM in detecting flooded landforms since the energy emitted by LiDAR (near infrared) is absorbed by water. Alternative methods should be considered to complete the mapping with the remaining flooded landforms, such as LiDAR signal intensity or ground point density analysis. Finally, 18 (32%) are truncated (e.g. cut by forest roads) or landforms that did not meet the filtering threshold values (i.e. depth less than 15 cm). Of the 350 shelters identified in the field, 306 were extracted from the LRM (87%). 44 shelters (13%) have been forgotten of which 5 (11%) are flooded shelters and 39 (89%) are undetected for the earlier mentioned reasons or because the LRM kernel size was not adapted to their size (shelters whose dimensions greatly exceed 6×6 m). Creating one or more LRMs from different kernel sizes is a way to solve this. Because detection statistics are satisfactory

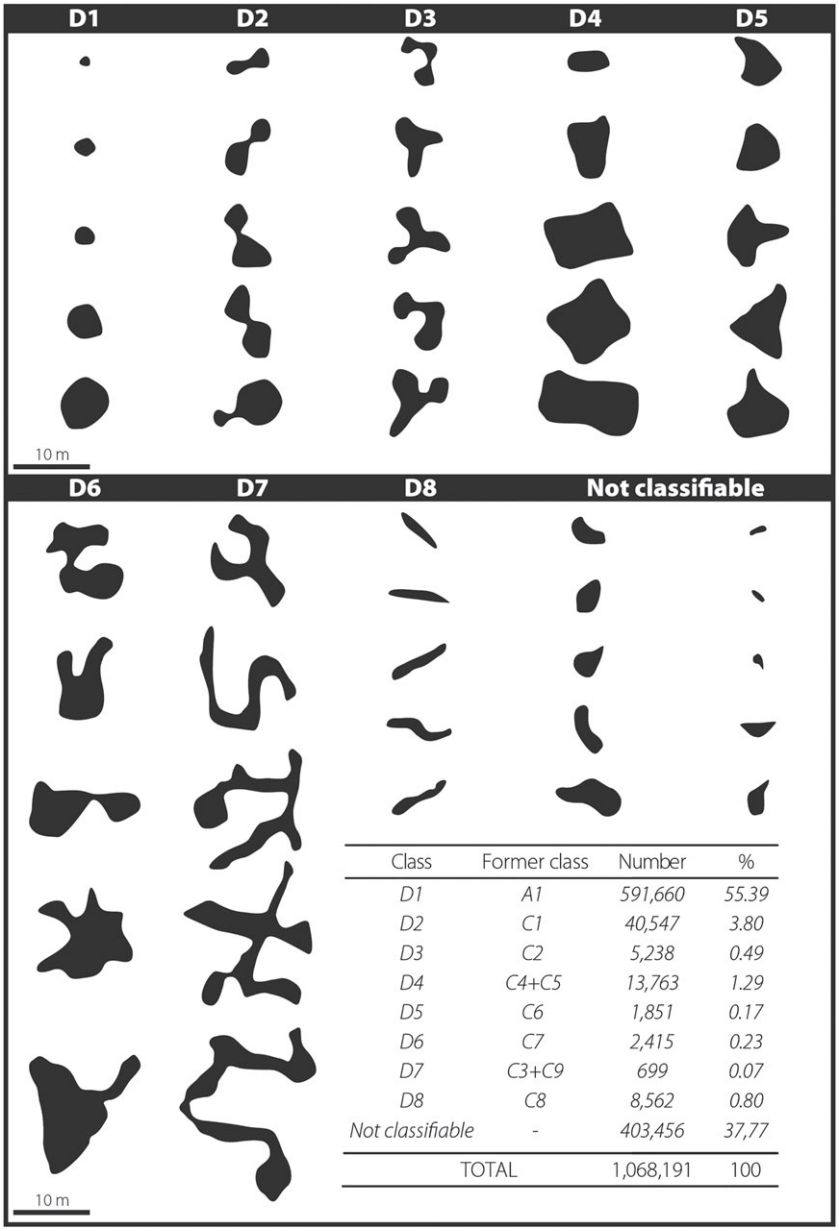

Class	Former class	Number	%
D1	*A1*	*591,660*	*55.39*
D2	*C1*	*40,547*	*3.80*
D3	*C2*	*5,238*	*0.49*
D4	*C4+C5*	*13,763*	*1.29*
D5	*C6*	*1,851*	*0.17*
D6	*C7*	*2,415*	*0.23*
D7	*C3+C9*	*699*	*0.07*
D8	*C8*	*8,562*	*0.80*
Not classifiable	-	*403,456*	*37,77*
	TOTAL	1,068,191	100

Figure 8. Final classification of the Verdun forest's landforms. D1: shell craters with one depression; D2: shell craters with two overlapped depressions; D3: shell craters with three or more overlapped depressions; D4: square shape and rectangular shelters; D5: triangular and semi-circular shelters; D6: diverse geometry shelters with great concavities; D7: pieces of trenches; D8: forest tracks, ditches and ruts. Each class is illustrated by five representative landforms (except for not classifiable landforms). Former class column represents number of class during classification process (before merging).

in terms of accuracy standards (88%), the method was implemented at the scale of the entire forest in order to obtain a ubiquitous vision of the number and distribution of war landforms.

Results

War landform inventory

Semi-automated polemoform mapping of the entire forest of Verdun demonstrated an overall effectiveness to detect the small-scale, sub-canopy landforms. For the 100 km^2 of the study area, 1 068 191 compact features were mapped after eliminating 243 749 landforms whose size did not exceed 1 m^2 (i.e. 1 311 940 landforms before sorting). Generally, the area histogram (Figure 7 and Table I) shows numerous features with a modest size since 75% of them have less than 6.3 m^2 area and half do not exceed 3.5 m^2 ($\overline{A}$=4.94). Conversely, few landforms (0.04%) are large and exceed 50 m^2 (A_{MAX}=263). In view of their elongation (Figure 7 and Table II), most of them are slightly elongated polygons since half are less than 0.02 and only 3% have a value greater than 0.05 and should be considered as linear. The solidity histogram (Figure 7 and Table II) also reveals the complexity of some landforms. Although compact objects are dominant (75% with *Sol*=0.99·1), 7% are formed by an irregular contour, indicating the presence of merged landforms (e.g. overlapped shell craters; shelter partially covered by a shell crater or by communication axis). If we look to the landforms profile, the depth histogram (Figure 7 and Table I) shows a predominance of shallow features ranging from 0.15 to 9.24 m ($\overline{D}$=0.57). Half do not reach 0.47 and 8% exceed 1 m. Among them, 5.3% have a particularly steep slope (S_{90}>30) and 0.4% a very steep slope (S_{90}>40).

Classification results and interpretation

The first classification (named A) of the million extracted features enabled us to distinguish three categories of landforms (Table III): circular, compact and low-slope landforms (A1); polygonal, compact and low-slope landforms (A2); and complex and/or elongated landforms with sinuous contour and moderate slope (A3). A1 consists of singular shell craters (overlapped shell craters are not detected in A; Figure 1). A2 and A3 provide landforms whose nature is undetermined because of their great geometric diversity (Asp_{MIN}=0.02; Asp_{MAX}=0.99; Cir_{MIN}=0.04; Cir_{MAX}=1). To refine it, a second classification was applied.

The second classification (named B), after setting aside A1 and merging A2 and A3, revealed four new landforms categories (Table IV): smooth shapes with low and regular slope (B1); marked landforms with moderate and regular slope (B2); marked landforms with steep and regular slope (B3); and salient shapes with steep and strongly concave slopes (B4). Because their profile is too far removed from the sampled soldier-made landforms, B1 and B2 landforms have been merged to include possible unbuilt features (overlapped shell craters, forest ditches, ruts, etc.) and soldier-made landforms whose profile has been flatted by bombings or post-war leveling. Regarding their salient profile (S_{90_MAX}=83.77), we suggest that B3 and B4 features are soldier-made landforms. Thus, both classes have been joined.

The third clustering (named C) allowed analyzing the shape variety of: (i) the unbuilt landforms (classes B1 and B2); and (ii) the soldier-made landforms (classes B3 and B4). The classification applied to B1 and B2 merged classes provides three categories of landforms (Table V): polygonal landforms with concavities (C1); elongated polygonal landforms with large concavities (C2); and linear landforms (C3). The classification conducted on B3 and B4 merged classes revealed six types of landforms (Table V): square and rectangular landforms (C4); rather rectangular landforms (C5); triangular and semicircular landforms (C6); polygonal landforms with large concavities (C7); elongated polygonal landforms (C8); and linear landforms (C9).

Based on the previous results, the typology of the Verdun forest's landforms is represented in eight distinct classes (named D; Figure 8 and 9) after including singular shell crater (class A1) and merging similar classes (C3 and C9, C4 and C5). Among 1 068 191 extracted landforms, 656 173 landforms (61%) could be considered as polemoforms (D1, D2, D3, D4, D5, D6 and D7). 8562 landforms (0.8%) constitute ditches and other features induced by forest management (D8). Furthermore, it should be noted that 403 456 landforms (38%) were not

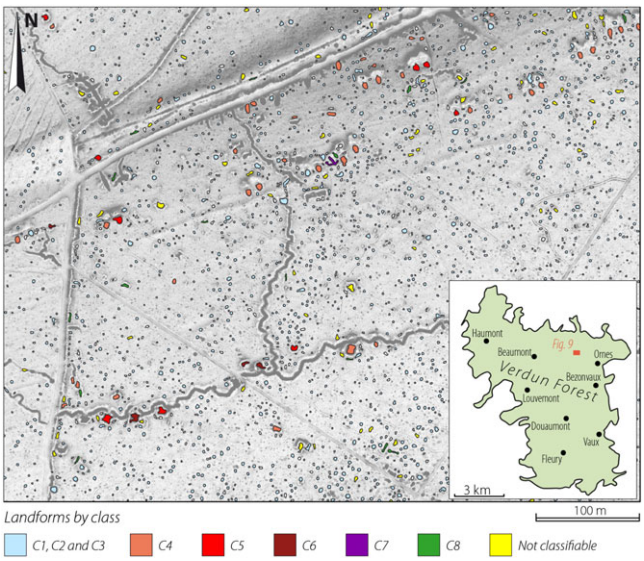

Figure 9. Extract of the landform inventory map west of Herbebois. This part of the battlefield is located on the German side around 5 km from the 1916 frontline and 1 km from the 1917–1918 frontline. It is covered by numerous small-size shell craters. We also observe 30 constructions organized according to a fire trench in the South. Great shelters are positioned along the trench while small dugouts are aligned and located more to the North in support of the first line. [Colour figure can be viewed at wileyonlinelibrary.com]

successfully interpreted because of their complex geometry (they were successively deleted after each classification). Concerning polemoform class interpretation (D1 to D7), class D1 is made of singular shell craters arising from a single strike. Class D2 contains overlapped shell craters with two depressions resulting from two close explosions. Class D3 groups overlapped shell craters with at least three depressions (three or more close explosions). Class D4 mainly consists of rectangular dugouts of variable sizes. They may also be underground dugout entrances or large depressions (A>100) used for bunker construction. Class D5 is composed of dugouts and gun positions whose aspect is pear-shaped or horseshoe (Figure 1). D6 mainly represents big size ammunition deposit, material shelters and gun positions ($\overline{A}$=17.98; A_{MAX}=218.16) with great concavities. Finally, D7 includes some trench sections (n=699; L_{F_MIN}=3.37; L_{F_MAX}=32.78).

For overlapped shell craters (D2 and D3), the number of observed craters must multiply the shell impact number. We can therefore consider that 81 094 shell craters were found in D2 and at least 15 714 appear in D3, bringing the total number of identified shell impacts to 688,468 in the Verdun forest, i.e. an average of 72 strikes/ha. At a time when LiDAR was not yet performed on the battlefield, Hupy and Schaetzl (2006) proposed an average number of 41 craters/ha recorded on the field for 10 plots of 0.25 ha each, which seems to be relatively closed to our estimates. Examination of strikes at a more local scale confirms this trend since they observed 86 impacts/ha near Fort Thiaumont while up to 120 impacts/ha were recorded in our study. Regarding the figures given by the artillerymen, the number of fired shells seems to be much more important than the above values. Assuming that 20 to 25% of ammunitions were defective (Hubé, 2016; Taborelli *et al.*, 2017a) over the 60 million fired during the Verdun battle (i.e. 12 million), an average of 4992 impacts/ha over the entire forest can be applied, recognizing that a significant number are non-explosive shells (no crater, e.g. gas and shrapnel shells). Overlapping craters, and

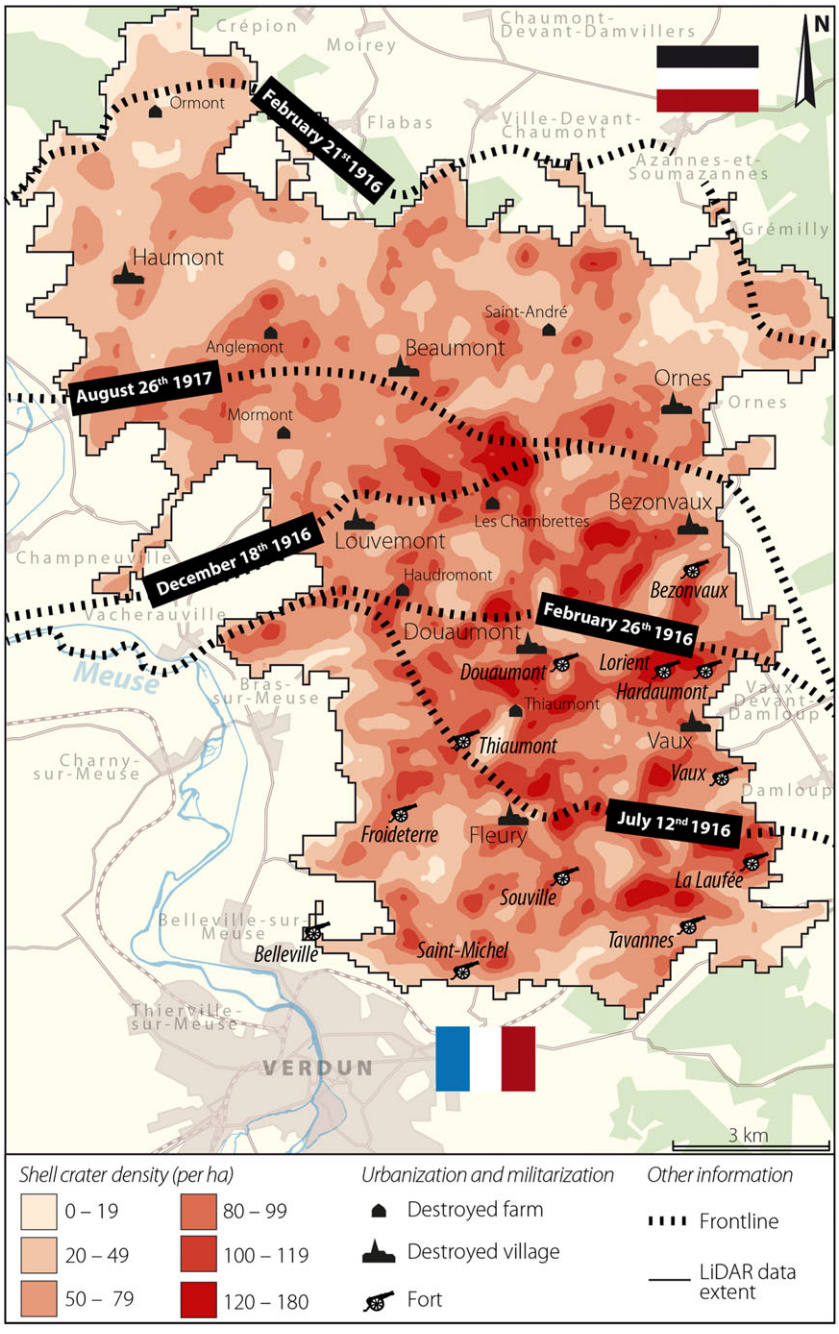

Figure 10. Shell crater density in the Verdun forest. [Colour figure can be viewed at wileyonlinelibrary.com]

craters within existing craters should also be taken into account, especially in the most targeted areas where it was common to observe a shell falling and exploding inside an existing crater (Hupy, 2006). In any case, these figures of different crater densities vary and should be construed as such, because study times and sampling methods differ. Rather, these estimates might be crossed to better assess the geomorphological impacts of war.

Spatial distribution of war landforms

Analysis of the battlefield using GIS software and spatial statistical methods revealed particular spatial patterns in the shell crater location (Figure 10). The most intensely disturbed area stands out south of the forest in the 'Quadrangle of the forts' (Fort Douaumont, Fort Vaux, Fort Souville and Fort Thiaumont), heart of the Verdun battle, and near Fort Hardaumont where significant impact densities are recorded: 100/ha at Fort Souville and up to 120/ha at Fort Douaumont which is by far the most affected fort (Pétain, 1986; Prost and Krumeich, 2015; Desrousseaux de Medrano, 2016). Other heavily damaged areas are prominent near the front line of September 1917, where fighting remained static until the end of the war. For example, an average of 180 impacts/ha were recorded around the Chambrettes farm, located on the top of a hill. In comparison, Brenot *et al*. (2017) counted up to 73 impacts/ha in Argonne and Note *et al*. (2018) found values approaching 480 impacts/ha in Flanders, demonstrating that crater density varies greatly according to proximity to the front. However, a 'polemological' gradient could be proposed to describe shell crater organization along the Western Front, where values increase from behind (in Verdun, northern and southern parts of the forest) to the first lines (in the center; Amat, 2001; Hupy, 2006; Figure 11).

The shelter density map (Figure 12) revealed much higher contrast in landform distribution within the Verdun forest with values from 0 to 19 constructions/ha and an average density of 1 construction/ha. Their location seems primarily controlled by the topographic factor (Figure 11) due to soldier settlement on the back slopes where the enemy could not see them (Barré, 1917; Hupy, 2006). This configuration is particularly noticeable through the famous ravines located west of Fort Douaumont, including the Death Ravine and Helly Ravine where up to 17 constructions/ha are recorded (Figure 13). Other construction clusters sprinkle the battlefield, for instance in the Cul Brûlé Ravine (up to 19 constructions/ha). Like the evoked 'polemological' gradient, a 'topographical' gradient can be proposed to describe the spatial distribution of soldier-made landforms, characterized by a constant density decrease from the slope base to the top, due to artillery fire exposure (Figure 11). The Ornes Twins outlier constitutes a blatant example whose relief allowed the Germans to hide their facilities on the northern slope. On the other hand, dissymmetry disappears in the center to make way for a more symmetrical configuration emerging from the passage of armed forces from both sides at different times (Pétain, 1986; Prost and Krumeich, 2015; Desrousseaux de Medrano, 2016). The biogeographical factor, although less noticeable, is also a key element in the battlefield organization (Amat, 2001, 2015). In that sense, forests played a major part in the concealment of the armies, unlike the farmed fields exposed in full view of the enemy. The use of these woodlands is particularly well illustrated in the Caures Wood where shelter density decreases significantly once beyond the forest edge (De Matos-Machado *et al*., 2016; Figure 12).

Other non-military factors may also affect polemoform distribution. Post-war construction of roadways and monuments related to the memorial aspect of the Verdun Battlefield has erased many of the war remnants on certain areas of the battlefield. Two areas notable for their lack of features located in the heart of the forest overlap the Wavrille shooting range (19 ha), the Douaumont Ossuary and the Fleury Necropolis (26 ha). In

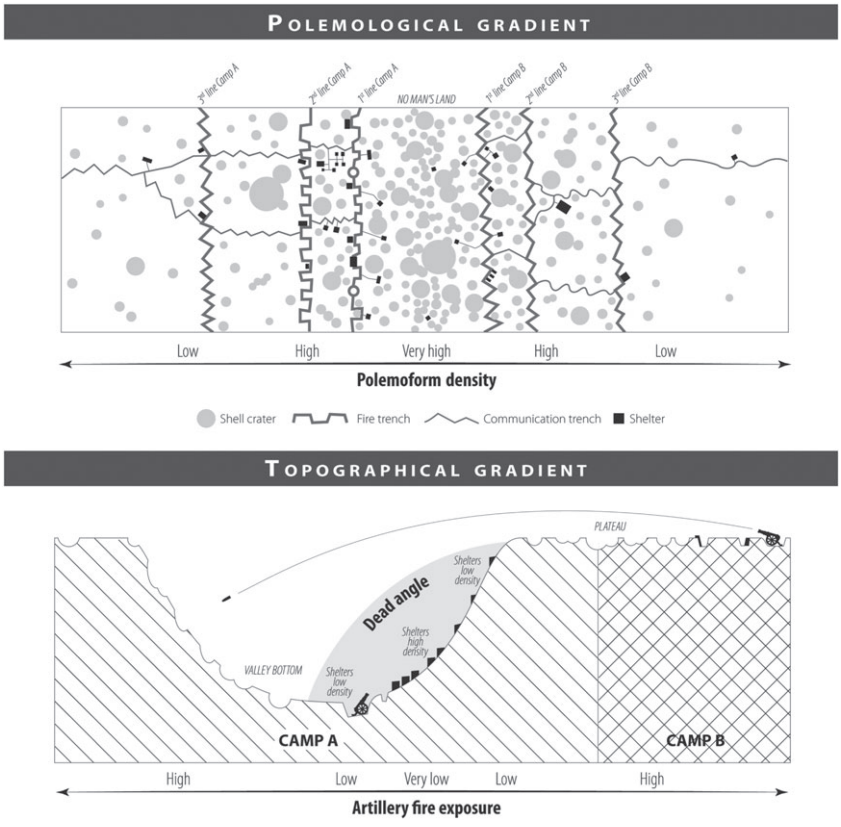

Figure 11. 'Polemological' and 'topographical' gradients.

addition, two-thirds of the forest were planted with coniferous trees (i.e. the pre-war farm lands) after foresters cleaned and leveled the ground to accommodate seedlings. Thus, polemoform density is notably lower in these plots (Amat, 2001, 2015; De Matos-Machado and Hupy, 2019). In close proximity to roads and monuments, landforms have been significantly altered by trampling and illicit archaeological excavations from the hundreds of thousands of visitors who come to the battlefield every year (Jacquemot and Legendre, 2011; Schnitzler and Landolt, 2013). Third, LiDAR technology did not allow us to fully detect the landforms contained by the coniferous and recently deciduous-planted lands. Because black pines and spruces are evergreen and beech seedlings are thick, the laser-beam associated with LiDAR technology does not penetrate through the canopy as well as other species, preventing some altimetric measurements on the ground (Devereux *et al.*, 2005; Doneus and Briese, 2011).

Volume quantification

Cross-checking of landforms maps and data tables permits quantification of landform volumes (Figure 14 and Table VI). Calculations conducted on the 2013 DTM revealed that at least 1.64 million m^3 of earth materials were displaced by shell explosions and defense constructions (not counting the volumes induced by trench excavation). Following the erosion processes that may have affected these landforms during the last century (leveling, trampling, colluviation, collapse, etc.), one could imagine that this amount was more important at the end of the war when landforms were still intact (Hupy, 2006; Brenot *et al.*, 2017). For each category of landform, disturbance shows that artillery deployed explosive munitions are by far the most destructive agent given that they alone contribute 81% to the battlefield erosion, representing an amount of 1.34 million m^3. In comparison, defense construction corresponds to only a

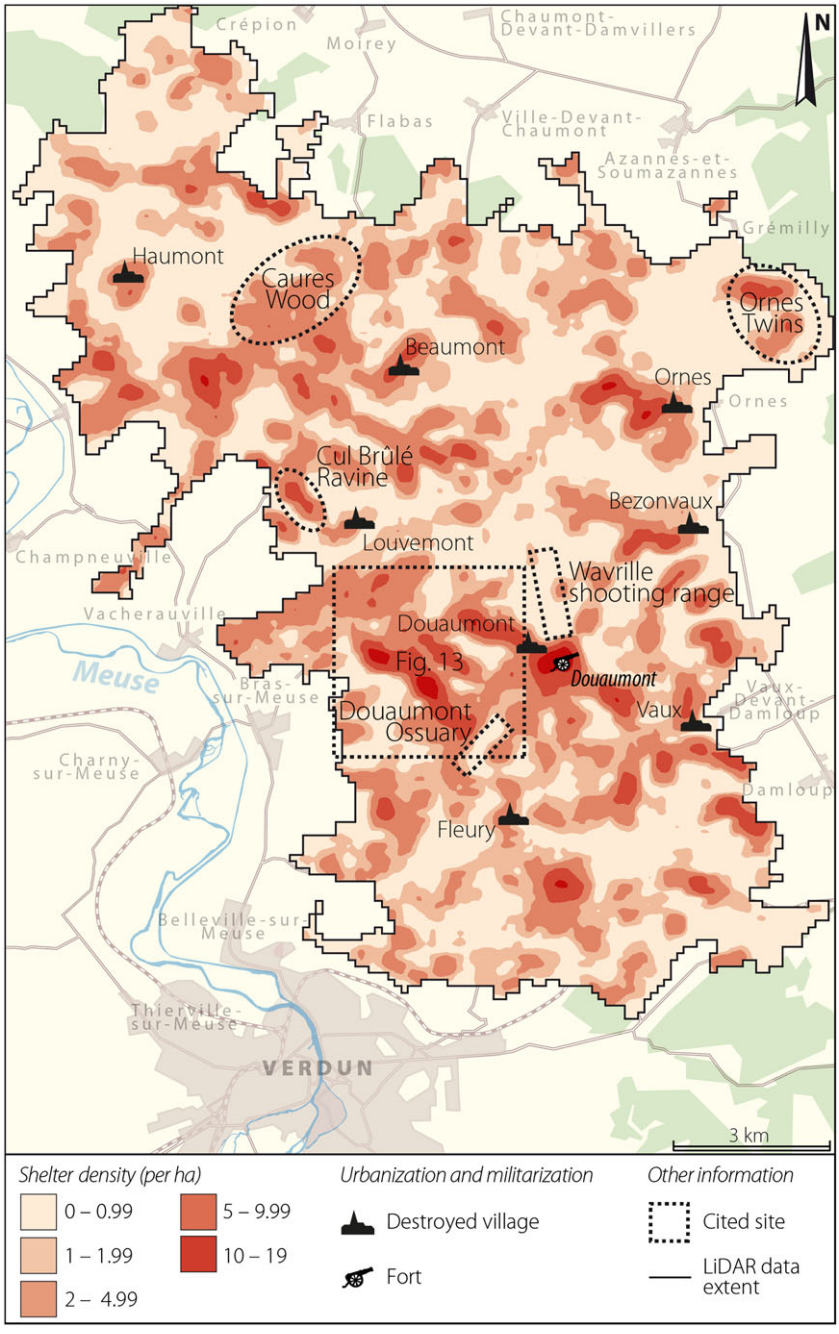

Figure 12. Shelter density in the Verdun forest. [Colour figure can be viewed at wileyonlinelibrary.com]

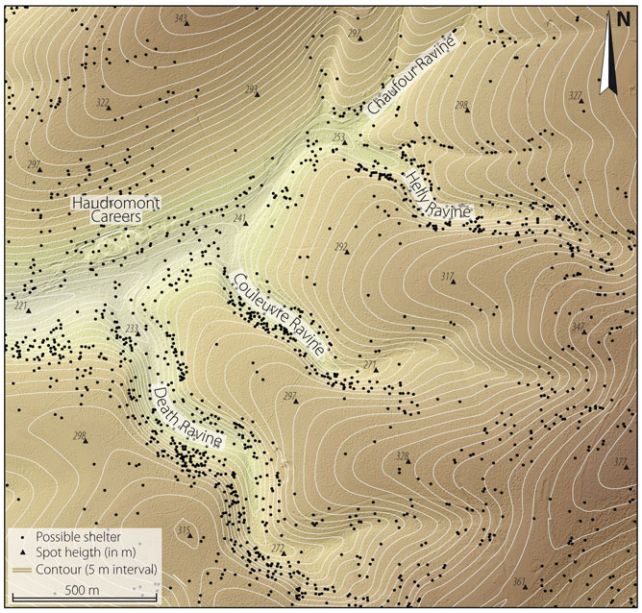

Figure 13. Shelter distribution west of Fort Douaumont. [Colour figure can be viewed at wileyonlinelibrary.com]

small part of the total measured volume, i.e. 0.30 million m^3 (19%). Finally, an average erosion of 170 m^3/ha can be suggested at the scale of the entire forest but with much higher values in locations subjected to the heaviest artillery bombardments (e.g. volumes reached 1680 m^3/ha near Fort Douaumont).

Discussion

Evaluation of landform classification

Classification using Kohonen's self-organizing maps and hierarchical agglomerative clustering resulted in the classification of 664 734 landforms (62%). However, the process was inefficient for the remaining 403 457 features (38%). According to the figures provided by the artillerymen (Pétain, 1986; Amat, 2001), it would seem obvious to consider that a large part of these unclassified landforms are shell craters. A primary reason behind this classification insufficiency is the small size of some landforms without distinct contour delineation, causing difficulties in identification. A second explanation of the inefficiency concerns nested landforms with a complex geometry making interpretation difficult. For example, in the heavily bombed areas of the forest center where the chaotic topography gave rise to alternating holes and bumps, polemoforms blend, and are difficult to identify as a singular distinct feature. Regarding our field experience, *in situ* interpretation using field survey can also be limited for the same reasons. Only archaeological artefacts found within these landforms (rare in greatly disturbed places), archaeological excavations (Jacquemot and Legendre, 2011; Passmore *et al*., 2013; Schnitzler and Landolt, 2013) or geophysical prospecting (Note *et al*., 2018) could allow us to interpret some of the remaining landforms. Overlaying historical documents with the DTM, such as ordnance survey maps (Plans directeurs – GQGA, 1917; Taborelli *et al*., 2017a) or aerial photographs (Stichelbaut, 2011; Stichelbaut et al., 2016a), may also be an alternative provided to combine German and French sources at different dates (information could vary by camp and time).

Among the polemoform-considered landforms (D1 to D7), 551 have been sampled in the field. The classification process correctly sorts 366 shell craters (93%) against 28 (7%) misclassified as shelter. With regard to the high detection rates and Hupy and Schaetzl observations (2006), crater classification seems to be reliable. Results are less accurate for shelters since 40 of them (25%) are likely shell craters whereas 117 (75%) are well classified as shelters. Thus, our figures overestimate the real number of shelters on the battlefield although validation was conducted on a small part of the landforms. In order to refine the results, several solutions are proposed. First, it might be interesting to analyze landforms topology to detect neighborhood relations between them. For example, a given landform will be more likely to be considered as shelter if its location is close to other shelters (spatial autocorrelation) and/or a trench. Moreover, it would be valuable to inspect the landform distribution because human occupations tend to be organized in space. Thus, clustering or alignment phenomena are locally observed allowing shelter recognition process. Finally, elevated landform location, not exploited in this study, could help to detect nearby cuttings, notably for underground dugouts where soldiers extracted great volumes of sediments.

Size variability of shell craters

Because craters are easily identified, and are by far the most studied war landforms, comparisons with other research are proposed in order to get an idea of their relative size. From the comparison of our results with other sites (two studies outside Verdun), we conclude that the size of the shell craters we observed is comparable with those encountered elsewhere:

- In the Gruerie Wood (France), Brenot *et al*. (2017) found shell crater sizes ranging from 1.13 to 7.61 m in diameter (*Me*=3.16 m) and 0.75 m in average depth.
- Near Fort Lusern (Italy), Magnini *et al*. (2017) sampled shell craters with dimensions close to those observed in Verdun: <1 m to >10 m wide and 0.5 to 2 m deep.

However, this brief comparative analysis is imperfect when we focus on mine craters whose morphometrics have been investigated in two other studies:

- On the *Chemin-des-Dames* (France), near Hill 108, Taborelli *et al*. (2017b) measured much larger landforms (mine craters) ranging from 10 to 89 m wide and from 10 to 22 m deep.
- In the Ypres Salient (Flanders, Belgium), Stichelbaut *et al*. (2016b) observed similar landforms varying from 10 to 75 m wide.

We also note that Verdun forest's landforms are comparable with those induced by aerial bombings from modern conflicts and it would be disproportionate to exclude them from this comparison. Thus, in the crater fields of the Andaines forest (Normandy), resulting from 13 June and 24 July 1944 bombings, Capps Tunwell *et al*. (2016) recorded landforms between 3.6 and 11.3 m in diameter (*Me*=7.9 m for site A; *Me*=8.2 m for site B) and between 1.5 and 3 m deep. Equally impressive but much deeper landforms have been observed in Vietnamese rice fields, where Westing and Pfeiffer (1972) proposed values ranging between 12 and 15 m in diameter and between 6 and 9 m in depth. In the Laotian landscapes, Kiernan (2015) recorded similar crater sizes around 10–12 m wide and 5 m deep.

Finally, it seems appropriate to extend this analysis through comparison of explosive munition shell craters with meteoritic craters, due to the striking similarity in shape between both

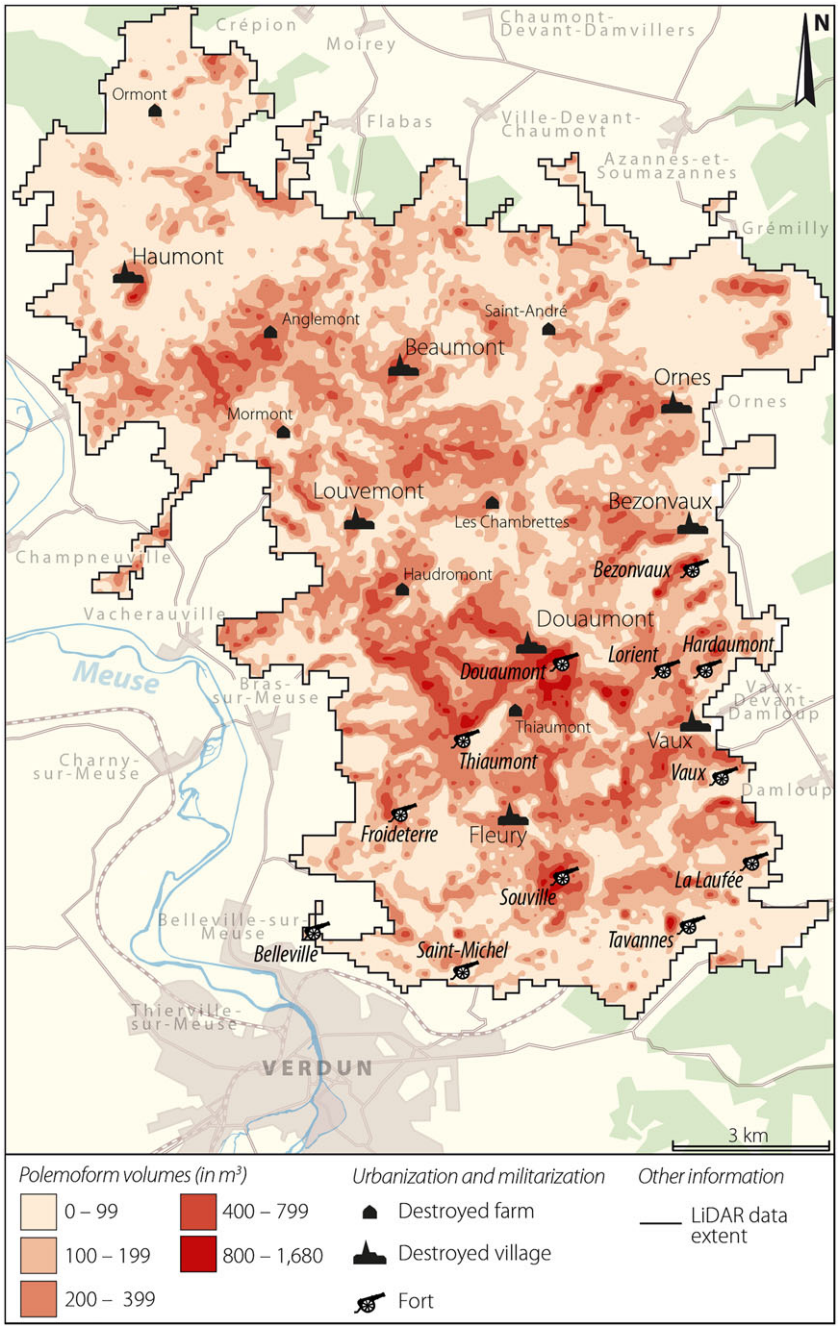

Figure 14. War-induced erosion in the Verdun forest (earth displaced sediments). [Colour figure can be viewed at wileyonlinelibrary.com]

Table VI. Polemoform volume quantification

Class	Landform type	Volume (millions of m^3)	%
D1	Shell craters with 1 depression	0.98	60
D2	Shell craters with 2 overlapped depressions	0.29	17
D3	Shell craters with 3 or + overlapped depressions	0.07	4
D4	Square shape and rectangular shelters	0.17	10
D5	Triangular and semi-circular shelters	0.04	2
D6	Diverse geometry shelters with great concavities	0.06	5
D7	Pieces of trenches	0.03	2
TOTAL		1.64	100

features. Using Salomon and Auly's astrobleme typology as reference (2010), comparisons reveal geometric similarities despite their differences in size: like shell craters, a large part of meteoritic craters (i.e. type A, the most common, induced by a vertical impact) are circular depressions surrounded by a more or less thick ejecta blanket. There are cases of merged craters, resulting from meteorite explosion during the crossing through the atmosphere (meteorite splits and disperses). Similarities are also observed in the morphogenesis that Melosh (1996) divided into three major phases: (i) contact and

compression; (ii) crater excavation; and (iii) crater modification (erosion processes after excavation).

Focusing on shell craters, several arguments explain such differences in value. Mention may be made of the type of explosive used. A 75 mm shell (6 kg of explosives) generates craters smaller than a 400 mm shell (90 kg). This relationship is exponential, reflecting rapid and continuous growth as the caliber increases. Crater size also depends on the pattern and setting. Shells equipped with a percussion fuse (explosion on the ground) leave stronger geomorphological traces than those provided with airburst fuse (explosion above the ground). The effect is more devastating when time fuses are used, because they penetrate sufficiently deep into the ground before explosion (Gascouin, 1921; Solard, 1935; Pétain, 1986; Prost and Krumeich, 2015). According to the observations made by Hupy (2006) on the Verdun battlefield, geology seems to be another parameter that affects landform dimensions. Craters tend to be deeper and steeper on weathered substrates and thick soils while active colluviation causes landforms to be filled in wet areas, making them wider than deep.

An original polemoform typology

Currently, few morphometric typologies of polemoform exist. Stichelbaut (2009) analyzed the shape variability of the trenches he observed in Flanders but did not classify shelters because of their low visibility on historical aerial photographs. Gheyle *et al*. (2018) completed Stichelbaut's typology through the use of LiDAR in the same area, suggesting different shelter geometries. Devos *et al*. (2015) and Taborelli *et al*. (2017b) also focused on trench geometries near Reims and in the Argonne Region and proposed a general polemoform typology without giving morphometric information. Finally, Passmore *et al*. (2013) proposed a WWII shelter classification in the Andaines Forest (France), where he identified by field survey eight types of shelter 1–14.5 m wide, 1.3–32.4 m long and 0.5–8 m deep. Consequently, our landform typology is innovative for WWI but not as a complete nomenclature since different types of landforms could be observed elsewhere, in particular through the re-use of our method on other WWI battlefields with accurate LiDAR data.

Volumes displaced by artillery fire

Regarding earth materials displaced by shells, estimates differ widely across the various regions intersected by the Western Front snaking across the landscape between 1914 and 1918. For the *Chemin-des-Dames*, Arnould and Simon (1994) state that between 110 and 185 m^3/ha of land were needed to fill craters, trenches and buried buildings. In the Gruerie Wood, Brenot *et al*. (2017) evoked erosion ranging from 219 to 1052 m^3/ha for shell craters only. In Flanders along 40 km of front line, an average erosion of 767 t/ha (i.e. 511 m^3/ha with a cubed weight of 1.5 t/m^3) is evoked for the same type of disturbance (Poesen, 2018). In the Argonne region and in the Aisne (Barisis Wood – *Bois de Barisis*), these theoretical volumes reach, respectively, 2000 m^3/ha (Arnould and Simon, 1994) and 2510 m^3/ha (Buridant, 2003), taking into account trench digging. Given the values we obtained (i.e. between 0 and 1680 m^3/ha, average 170 m^3/ha) and knowing that volumes related to trench digging are not included, we suggest that the Verdun battlefield can be considered as one of the most impacted site from a geomorphological point of view.

In order to compare the intensity of artillery-induced erosion with other soil erosion processes, we converted our estimates in t/ha/year. Thus, we consider a minimal erosion trend of 85 $t\,ha^{-1}\,a^{-1}$ on the Verdun battlefield (between February 1916 and November 1918) and up to 840 $t\,ha^{-1}\,a^{-1}$ near Fort Douaumont, the location most heavily bombarded. Arnaud-Fassetta (2003) and Lévêque (2003) gave figures on the load of suspended matter carried every year by several well-known rivers: 0.11 to 0.14 $t\,ha^{-1}\,a^{-1}$ of suspended matter recorded in the Rhine–Meuse delta; 0.7 $t\,ha^{-1}\,a^{-1}$ for the Amazon; 0.81 $t\,ha^{-1}\,a^{-1}$ for the Rhone; and 15 $t\,ha^{-1}\,a^{-1}$ for the Ganga. Poesen (2018) provided erosion rates related to various soil degradation processes: sugar beet cultivation causes a soil loss ranging from 0.1 to 44.4 $t\,ha^{-1}$ per harvest (in Europe); piping erosion is responsible for 0.96 to 287 $t\,ha^{-1}\,a^{-1}$ of soil loss (in Europe); sheet and rill erosion for 50 to 500 $t\,ha^{-1}\,a^{-1}$ (in the Global South). Considering the relative lowness of these figures, 'warfare should be recognized as a major erosion factor' (Poesen, 2018) as well as an integrated part of 'Anthropocene Geomorphology' studies (Goudie and Viles, 2016).

Conclusions

The use of LiDAR imagery on the Verdun forest greatly extended our knowledge of the Verdun battlefield. By using the canopy penetrating capabilities of LiDAR to see through the vegetative forest cover, an exhaustive method of mapping surviving shell craters and war remnants has been performed. At least 600 000 craters have been mapped, revealing the 'craterized' aspect of the Verdun battlefield. More than 18 000 possible shelters, now requiring ground-truthing measures, have been detected (excluding elevated concrete buildings) whereas the ONF identified only 261 features using field survey, completing the archaeological inventory of the Meuse department. In addition, this paper provides new information about geometry variability of war landforms since it demonstrates the existence of eight redundant shapes on the battlefield (including seven types of polemoform). Thus, spatial analysis of shell craters and shelter density showed a certain organization on the battlefield depending on their distance to the front line trenches and configuration to topographic relief.

Because the proposed method is readily useable by geographers (image processing and mapping using GIS, multivariate analysis with R®), it can be reproduced on other battlefields and other types of landforms. As a reminder, the method was first conducted at the scale of two sample sites representing 6% of the entire forest and was then successfully generalized at a speed much higher than a digitization based-method (the inventory and classification of 1 068 191 landforms would have required several months). Comparisons with other battlefields highlight the interest of such an initiative by revealing the existence of similarities between polemoforms issued from different battlefields (not only WWI). The extrapolation and adjustment of our methodology to other conflict landscapes is therefore possible taking into account the availability of LiDAR data or other kinds of topographical datasets. This is even more likely feasible since dozens of European conflict landscapes are now covered with high-resolution DTMs (e.g. Normandy, Argonne and Champagne forests in France, Ypres Salient and Ardennes forests in Belgium, Finnish Lapland, etc.). In addition, this methodology is not limited to simple polemoforms but also intends to investigate other similar types of landforms which can be anthropic such as charcoal kiln, burial mounds and pits (Trier and Pilø, 2012; Schneider *et al*., 2014; Trier *et al*., 2015) or natural such as karstic, volcanic and meteoritic landforms. However, our semi-automated detection algorithm presents

some limitations, especially in areas covered by numerous coalescent landforms (e.g. heavily bombarded forts in the case of WWI battlefields). Moreover, in order to allow optimal use of the proposed method, two conditions must be fulfilled: (i) LiDAR data must be detailed enough to accurately visualize landform contour geometry (e.g. a square shelter appears angular with a 20×20 cm pixel size whereas it becomes rounder with a 1×1 m pixel size). The ground point density, depending on both the number of emitted laser pulses per m^2 and vegetation density, must then be high enough to get a least one ground point for each 20×20 cm pixel; and (ii) the studied landforms must have a well-defined morphometric signature (the more angular and distinct the landforms are, the better the classification). The conservation state of the landforms is thus an important factor. In the case of areas perturbed by modern constructions, automatic classification can also be applied on georeferenced maps to remove the recently built landforms from the detection process.

As well as being directly applicable by scientists, the proposed method is intended to be used by local officials and others engaged in battlefield management efforts. Landform maps can help the ONF and the SRA to accurately assess the archaeological value of each plot in order to better take into account these historical issues that are involved in forest management planning. In addition, this body of research affords a means of ecological habitat detection (De Matos-Machado and Hupy, 2019) and plot accessibility information, helping foresters in their management works. Finally, these maps also supply direct applications of didactic nature to the public, in the image of the renovated Fleury Memorial, which was recently equipped with interactive screens allowing visitors to manipulate battlefield interpretation maps from this study.

Acknowledgements—The authors express their sincere thanks to the Grand Est's Regional Archaeology Department (SRA) of Metz and Gersende Gérard, Gérald Colin, René-Marc Pineau and Juliette Foltier of the Verdun's National Forests Office, for the provision of LiDAR data and maps of the forest planning. We are also grateful to Denis Jacquemot, Romain Perrier, Valentin Printemps, Théo Wohlschlegel and many others for their accompaniment on the field. We also thank the two reviewers and the assistant editor for their helpful and constructive comments that helped improve the manuscript.

References

Agarwal P, Skupin A (eds). 2008. *Self-Organising Maps: Applications in Geographic Information Science*. Chichester/Hoboken: Willey.

Amat J-P. 1987. Guerre et milieux naturels: les forêts meurtries de l'Est de la France, 70 ans après Verdun. *L'Espace Géographique* **16**(3): 217–233. https://doi.org/10.3406/spgeo.1987.4253.

Amat J-P. 2001. La forêt entre guerre et paix 1870–1995: étude de biogéographie historique sur l'Arc meusien de l'Argonne à la Woëvre. PhD thesis: Université Lille 1, Lille

Amat J-P. 2015. *Les forêts de la Grande Guerre: histoire, mémoire, patrimoine*. Presses de l'Université Paris-Sorbonne: Paris.

Arnaud-Fassetta G. 2003. River channel changes in the Rhone Delta (France) since the end of the Little Ice Age: geomorphological adjustment to hydroclimatic change and natural resource management. *Catena* **51**(2): 141–172. https://doi.org/10.1016/S0341-8162(02)00093-0.

Arnould P, Simon L. 1994. Forêts, guerre, après-guerre, autour du Chemin-des-Dames. In *Forêt et Guerre*, Corvol A, Amat J-P (eds). Éditions L'Harmattan: Paris; 251–270.

Barré C^{dr}. 1917. Organisation du terrain. Généralités et organisations défensives, Volume 1. École d'instruction du génie. http://gallica.bnf.fr/ark:/12148/bpt6k6532587h

Bater CW, Coops NC. 2009. Evaluating error associated with lidar-derived DEM interpolation. *Computers and Geosciences* **35**(2): 289–300. https://doi.org/10.1016/j.cageo.2008.09.001.

Brantz D. 2009. Environments of death: trench warfare on the Western Front, 1914–1918. In *War and the Environment: Military Destruction in the Modern Age*, Closmann C (ed). Texas A&M University Press: College Station; 68–91. https://muse.jhu.edu/book/12713.

Brenot J, Saulière N, Léty C, Taborelli P, Zélie B, Blondeau R, Devos A, Desfossés Y. 2017. How much did the soldiers dig? A quantification of WW1 remains in Argonne, France. *Geoarchaeology* **32**(5): 534–548. https://doi.org/10.1002/gea.21623.

Brown AG, Tooth S, Chiverrell RC, Rose J, Thomas DS, Wainwright J, Bullard JE, Thorndycraft VR, Aalto R, Downs P. 2013. The Anthropocene: is there a geomorphological case? *Earth Surface Processes and Landforms* **38**(4): 431–434. https://doi.org/10.1002/esp.3368.

Buridant J. 2003. La forêt mutilée – la reconstitution forestière dans l'Aisne après la Grande Guerre. *Graines d'Histoire, la Mémoire de l'Aisne* **17**: 13–24.

Capps Tunwell D, Passmore DG, Harrison S. 2016. Second World War bomb craters and the archaeology of Allied air attacks in the forests of the Normandie–Maine National Park, NW France. *Journal of Field Archaeology* **41**(3): 312–330. https://doi.org/10.1080/00934690.2016.1184930.

Celi M. 1991. The impact of bombs of World War I on limestone slopes of Monte Grappa. In *Proceedings of the International Conference on Environmental Changes in Karst Areas*, Bondesan A, Sauro U, Meneghel M (eds). IGU, UIS: Padua; 279–287.

Certini G, Scalenghe R, Woods WI. 2013. The impact of warfare on the soil environment. *Earth-Science Reviews* **127**: 1–15. https://doi.org/10.1016/j.earscirev.2013.08.009.

Challis K, Forlin P, Kincey M. 2011. A generic toolkit for the visualization of archaeological features on airborne LiDAR elevation data. *Archaeological Prospection* **18**: 279–289. https://doi.org/10.1002/arp.421.

Cochet F. 2014. *La Grande Guerre: Fin d'un Monde, Début d'un Siècle*. Perrin: Paris; 1914–1918.

De Matos-Machado R, Amat J-P, Arnaud-Fassetta G, Bétard F. 2016. Potentialités de l'outil LiDAR pour cartographier les vestiges de la Grande Guerre en milieu intra-forestier (bois des Caures, forêt domaniale de Verdun, Meuse). *EchoGéo* **38**: 1–22. https://doi.org/10.4000/echogeo.14791.

De Matos-Machado R, Hupy JP. 2019. The conflict landscape of Verdun, France: conserving cultural and natural heritage after WW1. In *Collateral Values: the Natural Capital Created by Landscapes of War*, Lookingbill T, Smallwood P (eds). Springer: New York, in press.

Desrousseaux de Medrano E (ed). 2016. *Dans la Bataille: Verdun 1916*. Nouvelles éditions: Jean-Michel Place, Paris.

Devereux BJ, Amable GS, Crow P, Cliff AD. 2005. The potential of airborne lidar for detection of archaeological features under woodland canopies. *Antiquity* **79**(305): 648–660. https://doi.org/10.1017/S0003598X00114589.

Devos A, Taborelli P, Dodici M, Chalumeau L, Buridant J, Bollot N, Combaud A, Desfossés Y. 2015. Rôle des conditions géographiques sur l'organisation spatiale des réseaux de défense de la Grande Guerre. Application à la Champagne (région de Reims). *Physio-Géo* **9**: 157–174. https://doi.org/10.4000/physio-geo.4615.

Doneus M, Briese C. 2011. Airborne laser scanning in forested areas – potential and limitations of an archaeological prospection technique. In *Remote Sensing for Archaeological Heritage Management. Proceedings of the 11th EAC heritage management symposium, Reykjavik*, Cowley D (ed), EAC Occasional Paper No. 5. Occasional Publication of the Aerial Archaeology Research Group No. 3. EAC: Brussels; 53–76.

Doyle P, Bennett MR. 1997. Military geography: terrain evaluation and the British Western Front 1914–1918. *The Geographical Journal* **163**(1): 1–24. https://doi.org/10.2307/3059682.

Doyle P, Bennett MR, Cocks F. 2000. Geology and warfare on the British sector of the Western Front 1914–1918. In *Geology and Warfare: Examples of the Influence of Terrain and Geologists on Military Operations*, Rose E, Nathanail C (eds). The Geological Society: Bath; 179–235.

Ehsani AH, Quiel F. 2009. Self-organizing maps for multi-scale morphometric feature identification using shuttle radar topography mission data. *Geocarto International* **24**(5): 335–355. https://doi.org/10.1080/10106040802642577.

Gascouin Gal. 1921. *L'Evolution de l'Artillerie Pendant la Guerre*. Flammarion: Paris.

Gheyle W, Stichelbaut B, Saey T, Note N, Van den Berghe H, Van Eetvelde V, Van Meirvenne M, Bourgeois J. 2018. Scratching the surface of war. Airborne laser scans of the Great War conflict landscape in Flanders (Belgium). *Applied Geography* **90**: 55–68. https://doi.org/10.1016/j.apgeog.2017.11.011.

Georges-Leroy M, Bock J, Dambrine E, Dupouey J-L. 2011. Apport du lidar à la connaissance de l'histoire de l'occupation du sol en forêt de Haye. *ArchéoSciences* **35**: 117–129. https://doi.org/10.4000/archeosciences.3015.

Goudie AS, Viles HA. 2016. *Geomorphology in the Anthropocene*. Cambridge University Press: Cambridge.

Grand Quartier Général des Armées Alliées. 1917. *Instruction sur les plans directeurs et les cartes et plans spéciaux*: GQGA, Paris. http://gallica.bnf.fr/ark:/12148/bpt6k6552158z.r=Instruction%20sur%20les%20plans%20directeurs%20et%20les%20cartes%20et%20plans%20spéciaux?rk=42918;4.

Hengl T, Reuter HI (eds). 2009. *Geomorphometry: Concepts, Software, Applications*. Elsevier: Amsterdam/Oxford.

Hesse R. 2010. LiDAR-derived local relief models – a new tool for archaeological prospection. *Archaeological Prospection* **17**(2): 67–72. https://doi.org/10.1002/arp.374.

Hesse R. 2014. Geomorphological traces of conflict in high-resolution elevation models. *Applied Geography* **46**: 11–20. https://doi.org/10.1016/j.apgeog.2013.10.004.

Hiller JK, Smith M. 2008. Residual relief separation: digital elevation model enhancement for geomorphological mapping. *Earth Surface Processes and Landforms* **33**: 2266–2276. https://doi.org/10.1002/esp.1659.

Hubé D. 2016. *Sur les Traces d'un Secret Enfoui: Enquête sur l'Héritage Toxique de la Grande Guerre*. Michalon: Paris.

Hupy JP. 2006. The long-term effects of explosive munitions on the WWI battlefield surface of Verdun, France. *Scottish Geographical Journal* **122**(3): 167–184. https://doi.org/10.1080/00369220618737264.

Hupy JP. 2011. Khe Sanh, Vietnam: examining the long-term impacts of warfare on the physical landscape. In *Modern Military Geography*, Palka E, Gal Gano F (eds). Routledge: New-York, London; 312–326.

Hupy JP, Schaetzl R. 2006. Introducing 'bombturbation', a singular type of soil disturbance and mixing. *Soil Science* **171**(11): 823–836. https://doi.org/10.1097/01.ss.0000228053.08087.19.

Hutchinson DJ, Diederichs M, Pehme P, Sawyer P, Robinson P, Puxley A, Robichaud H. 2008. Geomechanics stability assessment of World War I military excavations at the Canadian National Vimy Memorial Site, France. *International Journal of Rock Mechanics and Mining Sciences* **45**: 59–77. https://doi.org/10.1016/j.ijrmms.2007.04.014.

Ilyès Z. 2006. Military activities: warfare and defense. In *Anthropogenic Geomorphology: a Guide to Man-Made Landforms*, Szabo J, David L, Loczy D (eds). Springer: Dordrecht; 217–231.

Jacquemot S, Legendre J-P (eds). 2011. *Vestiges de Guerres en Lorraine: le Patrimoine des Conflits Mondiaux*. Metz: Éditions Serpenoise.

Kiernan K. 2015. Nature, severity and persistence of geomorphological damage caused by armed conflict. *Land Degradation and Development* **26**: 380–396. https://doi.org/10.1002/ldr.2216.

Kobiałka D, Kostyrko M, Wałdoch F. 2016. Archeologia II wojny światowej: materialne przekształcenia w krajobrazie leśnym wzdłuż rzeki Brdy (na odcinku od jeziora Śpierewnik do Rytla) związane z działaniami wojennymi w 1939 roku. *Zeszyty Chojnickie* **32**: 151–168.

Kokalj Ž, Zakšek K, Oštir K. 2011. Application of sky-view factor for the visualization of historic landscape features in lidar-derived relief models. *Antiquity* **85**(327): 263–273. https://doi.org/10.1017/S0003598X00067594.

Leibrandt S, Le Pennec J-L. 2015. Towards fast and routine analyses of volcanic ash morphometry for eruption surveillance applications. *Journal of Volcanology and Geothermal Research* **297**: 11–27. https://doi.org/10.1016/j.jvolgeores.2015.03.014.

Lévêque C. 2003. *Ecology: From Ecosystem to Biosphere*. Science Publishers: Enfield.

Liu EJ, Cashman KV, Rust AC. 2015. Optimising shape analysis to quantify volcanic ash morphology. *GeoResj* **8**: 14–30. https://doi.org/10.1016/j.grj.2015.09.001.

Magnini L, Bettineschi C, De Guio A. 2017. Object-based shell craters classification from LiDAR-derived sky-view factor. *Archaeological Prospection* **24**(3): 211–223. https://doi.org/10.1002/arp.1565.

Masson-Loodts I. 2014. *Paysages en Batailles. Les Séquelles Environnementales de la Grande Guerre*. Brussels: Éditions Nevicata.

Melosh HJ. 1996. *Impact Cratering: A Geologic Process*. Oxford University Press: Oxford.

Note N, Gheyle W, Van den Berghe H, Saey T, Bourgeois J, Van Eetvelde V, Van Meirvenne M, Stichelbaut B. 2018. A new evaluation approach of World War One's devastated front zone: a shell hole density map based on historical aerial photographs and validated by electromagnetic induction field measurements to link the metal shrapnel phenomenon. *Geoderma* **310**: 257–269. https://doi.org/10.1016/j.geoderma.2017.09.029.

Oja E, Kaski S (eds). 1999. *Kohonen Maps*. Elsevier: Amsterdam/London/Paris.

Olteanu-Raimond A-M, Ruas A. 2015. Carte de Kohonen et classification ascendante hiérarchique pour l'analyse de données géohistoriques. *Revue Internationale de Géomatique* **25**(4): 581–599. https://doi.org/10.3166/RIG.25.581-599.

Opitz RS, Cowley CD (eds). 2013. *Interpreting Archaeological Topography: 3D Data, Visualization and Observation*. Oxbow Books: Oxford.

Orians GH, Pfeiffer EW. 1970. Ecological effects of the war in Vietnam. *Science* **168**(3931): 544–554.

Passmore D, Capps Tunwell D, Harrison S. 2013. Landscapes of logistics: the archaeology and geography of WWII German military supply depots in Central Normandy, north–west France. *Journal of Conflict Archaeology* **8**(3): 165–192. https://doi.org/10.1179/1574077313Z.00000000025.

Pétain P. 1986. *La Bataille de Verdun*. Avalon: Paris.

Pittmann EW. 2000. Geologists and the American Civil War. In *Geology and Warfare: Examples of the Influence of Terrain and Geologists on Military Operations*, Rose E, Nathanail C (eds). The Geological Society: Bath; 84–106.

Poesen J. 2018. Soil Erosion in the Anthropocene: research needs. *Earth Surface Processes and Landforms* **43**: 64–84. https://doi.org/10.1002/esp.4250.

Printemps V. 2017. *Utilisation de l'outil LiDAR pour la détection des mares de la forêt domaniale de Verdun (Meuse)*. Université Paris-Diderot, Paris: Master thesis.

Prost A, Krumeich G. 2015. *Verdun, 1916: une Histoire Franco-Allemande de la Bataille*. Éditions Tallandier: Paris.

Relief Visualization Toolbox (RVT). 2015. http://iaps.zrc-sazu.si/node/67731#v

Salomon J-N, Auly T. 2010. Impacteurs et astroblèmes: essai de classification et approche géographique. *Géomorphologie: Relief, Processus, Environnement* **16**(1): 3–20. https://doi.org/10.4000/geomorphologie.7866.

Schneider A, Takla M, Nicolay A, Raab A, Raab T. 2014. A template-matching approach combining morphometric variables for automated mapping of charcoal kiln sites. *Archaeological Prospection* **22**(1): 45–62. https://doi.org/10.1002/arp.1497.

Schnitzler B, Landolt M (eds). 2013. *À l'est, du nouveau! Archéologie de la Grande Guerre en Alsace et en Lorraine*. Strasbourg: Éditions des Musées de la Ville de Strasbourg.

Solard C^{ne}. 1935. Fortification. La fortification pendant la guerre 1914–1918, Volume 2. *École d'Application d'Artillerie: Fontainebleau*. http://gallica.bnf.fr/ark:/12148/bpt6k65565434.r=Fortification.%20La%20fortification%20pendant%20la%20guerre%2019141918?rk=42918;4

Stal C, Bourgeois J, De Maeyer P, De Mulder G, De Wulf A, Goossens R, Nuttenst T, Stichelbaut B. 2010. Kemmelberg (Belgium) case study: comparison of DTM analysis methods for the detection of relicts from the First World War. In *Remote Sensing for Science, Education, and Natural and Cultural Heritage: Proceedings of the EARSeL Symposium 2010*, Reuter R (ed). European Association of Remote Sensing Laboratories (EARSeL). EARSeL: Strasbourg; 65–72.

Steinbach F, Husson J. 2007. Palimpsestes et héritages des polémopaysages dans les massifs du Saillant de Saint-Mihiel. In *La mémoire des forêts. Actes du colloque 'Forêt, archéologie et environnement'*, Dupouey J-L, Dambrine E, Dardignac C, Georges-Leroy M (eds). ONF, INRA, DRAC Lorraine: Nancy; 285–294.

Stevenson JA, Sun X, Mitchell NC. 2010. Despeckling SRTM and other topographic data with a denoising algorithm. *Geomorphology* **114**: 238–252. https://doi.org/10.1016/j.geomorph.2009.07.006.

Stichelbaut B. 2009. *World War One Aerial Photography: An Archaeological Perspective*. PhD thesis: Universiteit Gent, Gent.

Stichelbaut B. 2011. The first thirty kilometers of the western front 1914–1918: an aerial archaeological approach with historical remote sensing data. *Archaeological Prospection* **18**(1): 57–66. https://doi.org/10.1002/arp.397.

Stichelbaut B, Cowley D (eds). 2016a. *Conflict Landscapes and Archaeology from Above*. Ashgate Publishing: Farnham.

Stichelbaut B, Gheyle W, Saey T, Van Eetvelde V, Van Meirvenne M, Note N, Van den Berghe H, Bourgeois J. 2016b. The First World War from above and below. Historical aerial photographs and mine craters in the Ypres Salient. *Applied Geography* **66**: 64–72. https://doi.org/10.1016/j.apgeog.2015.11.020.

Štular B. 2011. The use of lidar-derived relief models in archaeological topography. The Kobarid region (Slovenia) case study. *Arheoloski Vestnik* **62**: 393–432. http://av.zrc-sazu.si/pdf/62/AV_62_2011_Stular.pdf.

Štular B, Kokalj Ž, Oštir K, Nuninger L. 2012. Visualization of lidar-derived models for detection of archaeological features. *Journal of Archaeological Science* **39**(11): 3354–3360. https://doi.org/10.1016/j.jas.2012.05.029.

Sun X, Rosin PL, Martin RR, Langbein FC. 2007. Fast and effective feature-preserving mesh denoising. *IEEE Transactions Visualization and Computer Graphics* **13**(5): 925–938. https://doi.org/10.1109/TVCG.2007.1065.

Taborelli P, Bollot N, Devos A, Dodici M, Desfossés Y. 2016. Apport des plans directeurs sur la compréhension de l'organisation spatiale du front durant la Grande Guerre. Application à l'Argonne. *Revue de Géographie Historique* **8**. http://rgh.univ-lorraine.fr/articles/view/66/.

Taborelli P, Devos A, Laratte S, Brenot J, Bollot N, Cancès B, Desfossés Y. 2017a. Apport des plans directeurs et de l'outil LiDAR aéroporté pour la caractérisation des impacts morphologiques de la Grande Guerre: exemple de la cote 108 (Berry-au-Bac, France). *Géomorphologie: Relief, Processus, Environnement* **23**(2): 155–169. https://doi.org/10.4000/geomorphologie.11711.

Taborelli P, Devos A, Laratte S, Desfossés Y, Brenot J. 2017b. Typologie et organisation spatiale des 'polémo-formes' de la Grande Guerre révélées par l'outil LiDAR et les Plans directeurs. Application à la Champagne et à l'Argonne. *Revue de Géographie Historique* **10–11**. http://rgh.univ-lorraine.fr/articles/view/88/.

Tarolli P. 2016. Humans and the Earth's surface. *Earth Surface Processes and Landforms* **41**(15): 2301–2304. https://doi.org/10.1002/esp.4059.

Toumazet J-P, Vautier F, Roussel E, Dousteyssier B. 2017. Automatic detection of complex archaeological grazing structures using airborne laser scanning data. *Journal of Archaeological Science: Reports* **12**: 569–579. https://doi.org/10.1016/j.jasrep.2017.03.012.

Trier ØD, Pilø LH. 2012. Automatic detection of pit structures in airborne laser scanning data. *Archaeological Prospection* **19**(2): 103–121. https://doi.org/10.1002/arp.1421.

Trier ØD, Zortea M, Tonning C. 2015. Automatic detection of mound structures in airborne laser scanning data. *Journal of Archaeological Science: Reports* **2**: 69–79. https://doi.org/10.1016/j.jasrep.2015.01.005.

Unglert K, Radić V, Jellinek AM. 2016. Principal component analysis vs self-organizing maps combined with hierarchical clustering for pattern recognition in volcano spectra. *Journal of Volcanology and Geothermal Research* **21**(5): 58–74. https://doi.org/10.1016/j.jvolgeores.2016.04.014.

Van der Schriek M, Beex W. 2017. The application of LiDAR-based e_k; DEMs on WWII conflict sites in the Netherlands. *Journal of Conflict Archaeology* **12**(2): 94–114. https://doi.org/10.1080/15740773.2017.1440960.

Wehrens R, Buydens LMC. 2007. Self- and Super-organizing Maps in R: the kohonen Package. *Journal of Statistical Software* **21**(5): 1–19. https://econpapers.repec.org/article/jssjstsof/v_3a021_3ai05.htm.

Westing AH. 1975. Environmental consequences of the second Indochina war: a case study. *Ambio* **4**(5–6): 216–222. http://www.jstor.org/stable/4312150.

Westing AH, Pfeiffer E. 1972. The cratering of Indochina. *Scientific American* **226**(5): 21–29.

Westing AH. 2013. *Arthur H. Westing: Pioneer on the Environmental Impact of War*. Springer: Berlin/Heidelberg. https://doi.org/10.1007/978-3-642-31322-6

Wulder MA, White JC, Nelson RF, Næsset E, Ørka HO, Coops NC, Hilker T, Bater CW, Gobakken T. 2012. Lidar sampling for large-area forest characterization: a review. *Remote Sensing of Environment* **121**: 196–209. https://doi.org/10.1016/j.rse.2012.02.001.

Zakšek K, Oštir K, Kokalj Ž. 2011. Sky-view factor as a relief visualization technique. *Remote Sensing* **3**: 398–415. https://doi.org/10.3390/rs3020398.

